

École doctorale n° 364 : Sciences Fondamentales et Appliquées

Doctorat ParisTech

THÈSE

pour obtenir le grade de docteur délivré par

l'École Nationale Supérieure des Mines de Paris

Spécialité doctorale “Science et Génie des Matériaux”

présentée et soutenue publiquement par

Ali SAAD

le 26 avril 2015

NUMERICAL MODELLING OF MACROSEGREGATION INDUCED BY SOLIDIFICATION SHRINKAGE IN A LEVEL SET APPROACH

Directeurs de thèse: **Michel BELLET**
Charles-André GANDIN

Jury

M. Vincent Vega,	Professeur, MINES ParisTech	Rapporteur
M. Jules Winnfield,	Professeur, Arts Et Métiers ParisTech	Rapporteur
M. Butch Coolidge,	Chargé de recherche, ENS Cachan	Examinateur
Mme. Mya Wallace,	Danseuse, en freelance	Examinateur
M. Marsellus Wallace,	Ingénieur, MIT	Examinateur

T
H
E
S
S

Contents

1 General Introduction	1
1.1 Casting defects	2
1.2 Macrosegregation	3
1.2.1 Causes	4
1.2.2 Types	5
1.3 Industrial Worries	7
1.4 Project context and objectives	8
1.4.1 Context	8
1.4.2 Objectives and outline	9
2 Modelling Review	11
2.1 Modelling macrosegregation	12
2.1.1 Dendritic growth	12
2.1.2 Mush permeability	13
2.1.3 Microsegregation	13
2.1.4 Macroscopic solidification model: monodomain	16
2.2 Eulerian and Lagrangian motion description	18
2.2.1 Overview	18
2.2.2 Interface capturing	19
2.3 Solidification models with level set	19
2.4 The level set method	20
2.4.1 Transport and reiniliaztion	20
2.4.2 Interface Remeshing	20
2.4.3 Mixing Laws	20
3 Energy balance with thermodynamic tabulations	21
3.1 State of the art	22
3.2 Thermodynamic considerations	22
3.2.1 Volume averaging	22
3.2.2 The temperature-enthalpy relationship	23
3.2.3 Tabulation of properties	23
3.3 Formulation	25
3.4 Validation	25

Contents

3.4.1	Pure diffusion	25
3.4.2	Convection-diffusion with macrosegregation	25
4	Macrosegregation with incompressible fluid motion	29
4.1	Introduction	30
4.2	Review fluid mechanics	30
4.3	VMS solver	30
4.4	Computational stability	30
4.4.1	Integration order	30
4.5	Application to multicomponent alloys	31
4.5.1	Tabulations	31
4.6	Macroscopic freckle prediction	33
4.6.1	Introduction	33
4.6.2	Experimental work	33
4.6.3	Macroscopic scale simulations	33
4.7	Meso-Macro Freckle prediction	34
5	Macrosegregation with solidification shrinkage	35
5.1	Literature review	36
5.2	Level set treatment	36
5.2.1	Permeability mixing	36
5.3	Conservation equations	37
5.3.1	Mass Conservation	37
5.3.2	Momentum Conservation	38
5.3.3	Energy Conservation	41
5.3.4	Species Conservation	43
5.4	Test cases	44
5.4.1	Validation of LS transport	44
5.4.2	Shrinkage without macrosegregation	44
6	Macrosegregation with shrinkage and deformable solid OR Application to TEXUS	45
Conclusion and Perspectives		47
Appendix A Notes		49
A.1	Useful Expressions	49
Bibliography		51

Acronym	Standing for
ALE	Arbitrary Lagrangian-Eulerian
CCEMLCC	Chill Cooling for the Electro-Magnetic Levitator in relation with Continuous Casting of steel
CEMEF	Center for Material Forming
DLR	Deutsches Zentrum für Luft- und Raumfahrt
EML	Electromagnetic levitation
ESA	European Space Agency
FEM	Finite Element Method
ISS	International Space Station
IWT	Institut für Werkstofftechnik
LHS	Left Hand Side
MAC	Marker-and-cell
PF	Phase field
RHS	Right Hand Side
RUB	Ruhr Universität Bochum
RVE	Representative Elementary Volume
VOF	Volume Of Fluid

Contents

Chapter 1

General Introduction

Macrosegregation is a very known defect to metallurgical processes. Despite a great evolution achieved by active research during the last 60 years, it remains partially understood. Macrosegregation is often the consequence of several factors at the scale of a casting, all related to *microsegregation* happening at the scale of dendrites. Today, research in metallurgy focuses on a deeper understanding of such a connection between the different physical scales. Solidification is not only a phase change, but also a complex transformation involving small scales like nucleation, medium scales like grains growth and large scales like convection in the melt. From the nucleation theory to the mechanical behavior of metals, intricate phenomena combine to form defects in the final product. This has been seen in casting processes, such as continuous casting (fig. 1.1) and ingot casting. Surface and volume porosity, hot tearing and composition heterogeneity are known defects to the casting community. After a brief introduction of these defects, macrosegregation will be the focus of this dissertation.



Fig. 1.1 – Main steps in a continuous casting plant

1.1 Casting defects

Undesired effects are inevitable in any industrial process. More importantly, a lot of defects in the casting industry can be disastrous in some situations where the cast product is not serviceable and hence rejected. This leads to a systematic product recycling, i.e. the product is ditched to be reheated, remelted and then cast again. From an economic point view, the operation is expensive timewise and profitwise. Understanding and preventing defects when possible, is thus crucial in the casting industry. We focus hereafter on the main encountered defects.

Hot tearing

This defect, also denoted solidification cracking or hot cracking, occurs in the mushy zone at high solid fractions when a failure or crack appears at specific locations, the hot spots. The temperature range in which the steel is vulnerable to hot tearing is known as the brittleness temperature range (BTR). It corresponds to solid fractions greater than 90%, with the liquid phase forming a discontinuous film. Many factors can cause the failure, but the main origin is a lack of liquid feeding required to compensate for the solidification shrinkage, in the presence of thermal stresses in the mushy region. Therefore, a crack initiates then propagates in the casting, as shown in [fig. 1.2](#).



Fig. 1.2 – Crack in an aluminium slab

Porosity

Porosity is a void defect formed inside the casting or at the outer surface. It may attributed to two different factors. Firstly, we speak of *shrinkage porosity*, when a void forms as a result of density differences between the interdendritic liquid and solid network, the latter being denser than the former ([figs. 1.3c and 1.3d](#)). It is basically, the same reason that initiates hot cracks. The second factor is the presence of dissolved gaseous phases in the melt ([figs. 1.3a and 1.3b](#)). According to [Dantzig et al. \[2009\]](#), these gases may be initially in the melt, or created by the reaction between the metal and water found in the air or at trapped in grooves at the moulds surface. If the decreasing temperature and pressure drop in the liquid are large

enough, the latter becomes supersaturated. Consequently, the nucleation of gaseous phase is triggered (just like when you open a cold bottle of coca-cola is opened!).



Fig. 1.3 – Examples of porosity in casting and welding

Freckles or segregated channels

The origin of this defect is a combined effect of microsegregation and buoyancy forces. Upon solidification, solid forms while rejecting some solute in the liquid due to partitioning (steels have a partition coefficient less than unity). When segregated solute is the lighter species, an increasing concentration in the liquid phase produces a solutal driving force inside the mushy zone, generating unstable convection currents, with "plume" shapes as often reported in the literature [Sarazin et al. 1992; Schneider et al. 1997; Shevchenko et al. 2013]. When temperature gradient is an additional force of convection, the latter is hence qualified as "thermosolutal".

1.2 Macrosegregation

Macrosegregation generally stems from a solubility difference between a liquid phase and one or more solid phases, along with a relative velocity between these phases. While the former is responsible for local solute enrichment or depletion, the latter will propagate the composition heterogeneity on a scale much larger than just a few dendrites. This is why macrosegregation could be observed on the scale of a casting, up to several meters in length.

While microsegregation can be healed by annealing the alloy to speed up the diffusion process and allow homogenization, heterogeneities spanning on larger distances cannot be treated after solidification. It is obvious that macrosegregation is irreversible defect. Failure to prevent it may lead to a substantial decline in the alloy's mechanical behavior, hence its serviceability.

1.2.1 Causes

Four main factors can (simultaneously) cause fluid flow leading to macrosegregation:

Liquid dynamics

During solidification, thermal and solutal gradients result in density gradients in the liquid phase:

$$\rho^l = \rho_{\text{ref}}(1 - \beta_T(T - T_{\text{ref}}) - \sum_i \beta_{w_i^l}(w_i^l - \langle w_i \rangle_{\text{ref}}^l)) \quad (1.1a)$$

$$\vec{\nabla} \rho^l = -\rho_{\text{ref}}(\beta_T \vec{\nabla} T + \sum_i \beta_{w_i^l} \vec{\nabla} w_i^l) \quad (1.1b)$$

In eq. (1.1a), density is assumed to vary linearly with temperature and phase composition for each chemical species (index i). The slopes defining such variations are respectively the thermal expansion coefficient β_T and solutal expansion coefficient $\beta_{w_i^l}$, given by [Kohler 2008]:

$$\beta_T = -\frac{1}{\rho_{\text{ref}}} \left(\frac{\partial \rho^l}{\partial T} \right) \quad (1.2a)$$

$$\beta_{w_i^l} = -\frac{1}{\rho_{\text{ref}}} \left(\frac{\partial \rho^l}{\partial w_i^l} \right) \quad (1.2b)$$

The linear fit assumes also that the density takes a reference value, ρ_{ref} , when temperature and liquid composition reach reference values, respectively T_{ref} and $\langle w_i \rangle_{\text{ref}}^l$. However, in some situations, a suitable thermodynamic database providing accurate density values is far better than a linear fit, especially in the current context of macrosegregation. Such possibility will be discussed later in the manuscript (cf. SECTION TODO). In the presence of gravity, the density gradient in eq. (1.1b), causes thermosolutal convection in the liquid bulk and a subsequent macrosegregation.

Solidification shrinkage

Solid alloys have a greater density than the liquid phase ($\rho^s > \rho^l$), thus occupy less volume. Upon solidification, the liquid moves towards the solidification front to compensate for the volume difference caused by the phase change, as well as the thermal contraction. When macrosegregation is triggered by solidification shrinkage, we speak of *inverse segregation*. Theoretically, if solute mass is conserved, a decreasing volume results in a positive segregation. Shrinkage deforms the outer surface of a solidifying alloy, causing positive macrosegregation.

While one would naturally expect negative macrosegregation in areas where solidification begins and positive inside the alloy, shrinkage promotes the opposite phenomenon, hence the term *inverse segregation*. In contrast to liquid convection, shrinkage flow may cause macrosegregation even without gravity.

Movement of equiaxed grains

Equiaxed grains can grow in the liquid bulk where thermal gradients are weak, or in the presence of inoculants. Consequently, they are transported by the flow (floating or sedimenting, depending on their density [Beckermann 2002]) which leads to negative macrosegregation in their final position.

Solid deformation

Stresses of thermal and mechanical nature are always found in casting processes (e.g. bulging between rolls in continuous casting). Deformation of the semi-solid in the mushy zone causes a relative solid-liquid flow in the inward (tensile stresses) or outward (compression stresses) direction, causing macrosegregation.

1.2.2 Types

In continuous casting

The semi-solid billet is carried through a series of rolls that exert a radial force to straighten it and get it to its horizontal position. As the mushy part of a slab enters through these rolls, interdendritic liquid is expelled backwards, i.e. regions with lower solid fraction. Since the boundaries solidify earlier than the centre, the enriched liquid accumulates halfway in thickness, forming a centreline macrosegregation as shown in [fig. 1.4](#). Other types of segregates (channels, A-segregates ...) can also be found but remain more specific to ingot casting.

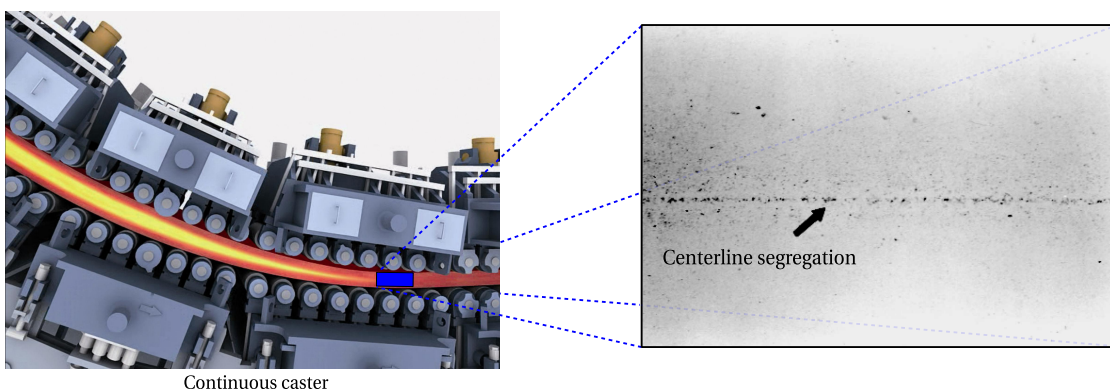


Fig. 1.4 – Centreline segregation in a steel slab [Beckermann 2002]

In ingot casting

A variety of segregation patterns can be encountered in heavy ingots:

- the lower part is characterized by a negative segregation cone promoted by the sedimentation of equiaxed crystals,
- positive segregation channels, known as A-segregates, form along the columnar dendritic zones, close to the vertical contact with the mould,
- positive V-segregates can be identified in the centre of the ingot,
- a positive macrosegregation in the upper zone where the last liquid solidifies, the so-called "hot-top", caused by solidification shrinkage (inverse segregation) and thermosolutal buoyancy forces.

Combeau et al. [2009] state that A-segregates and V-segregates formation is mainly attributed to local flow phenomena. As such, their scale is finer than macrosegregation, hence called "mesosegregates".



Fig. 1.5 – Sulphur print (left) of a 65-ton steel ingot [Lesoult 2005] showing various patterns (right) of macrosegregation [Flemings 1974]

In investment casting

This process is widely used to cast single-crystal (SC) alloys for turbines and other applications that require excellent mechanical behavior [Giamei et al. 1970]. During directional solidification, thermosolutal forces thrust segregated species outside of the mushy zone into the liquid bulk. The segregation scale ranges from a few dendrites to a few hundreds of them, hence forming "long and narrow trails" (fig. 1.6a) as described by Felicelli et al. [1991]. Freckles are frequently formed by small equiaxed grains (fig. 1.6b), probably caused by a uniform temperature gradient that settles as the channels become richer in solute. They can be observed on the ingot's surface, as well as in the volume.

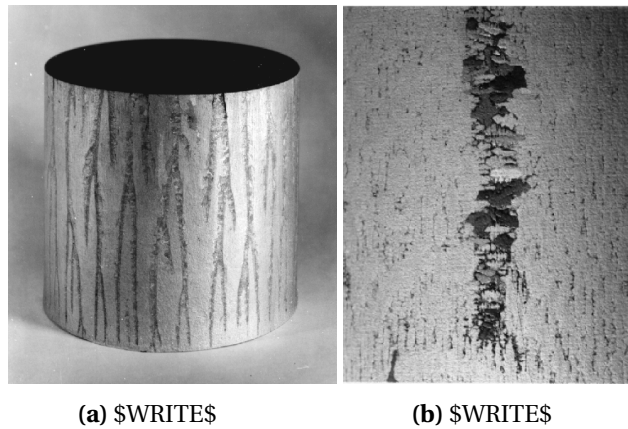


Fig. 1.6 – Freckles in directional casting of nickel-base superalloys

1.3 Industrial Worries

Steel production has continuously increased over the years to meet the industrial needs. [Figure 1.7](#) shows this increase between 1980 and 2013 with a clear dominance of the Chinese production. Quality constraints have also increased where specific grades of steel are needed in critical applications such as mega-structures in construction and heavy machinery. Therefore, alloys with defects are considered vulnerable and should be avoided as much as possible during the casting process. As such, steelmakers have been investing in research, with the aim of understanding better the phenomena leading to casting problems, and improve the processes when possible.



Fig. 1.7 – Evolution curves of crude steel worldwide production from 1980 to 2013

Simulation software dedicated to alloy casting is one of the main research investments undertaken by steelmakers. These tools coming from academic research are actively used to optimize the process. However, few are the tools that take into account the casting environ-

Chapter 1. General Introduction

ment. For instance, the continuous casting process, in [fig. 1.1](#), is a chain process where the last steps involve rolls, water sprays and other components. A dedicated software is one that can provide the geometric requirements with suitable meshing capabilities, as well as respond to metallurgical and mechanical requirements, mainly:

- handling moulds and their interaction with the alloy (thermal resistances ...)
- handling alloy filling and predicting velocity in the liquid and mushy zone
- handling thermomechanical stresses in the solid
- handling multicomponent alloys and predicting macrosegregation
- handling finite solute diffusion in solid phases
- handling real alloy properties (not just constant thermophysical/thermomechanical properties)

1.4 Project context and objectives

1.4.1 Context

The European Space Agency (ESA) has been actively committed, since its foundation in 1975, in the research field. Its covers not only exclusive space applications, but also fundamental science like solidification. This thesis takes part of the ESA project entitled *CCEMLCC*, abbreviating "Chill Cooling for the Electro-Magnetic Levitator in relation with Continuous Casting of steel". The three-year contract from 2011 to late 2014 denoted *CCEMLCC II*, was preceded by an initial project phase, *CCEMLCC I*, from 2007 to 2009. The main focus is studying containerless solidification of steel under microgravity conditions. A chill plate is later used to extract heat from the alloy, simulating the contact effect with a mould in continuous casting or ingot casting. A partnership of 7 industrial and academic entities was formed in *CCEMLCC II*. A brief summary of each partner's commitment:

Academic partners

- CEMEF (France): numerical modelling of microgravity chill cooling experiments
- DLR (German Aerospace Centre) and RUB university (Germany): preparation of a chill cooling device for electromagnetic levitation (EML), microgravity testing and investigation of growth kinetics in chill-cooled and undercooled steel alloys
- University of Alberta (Canada): impulse atomization of the D2 tool steel
- University of Bremen - IWT institute (Germany): study of melt solidification in atomization processing

Industrial partners

- ARCELORMITTAL (France): elaboration of a series of steel grades used in microgravity and ground studies

- METSO Minerals Inc. (Finland): material production with D2 tool steel for spray forming
- TRANSVALOR (France): development and marketing of casting simulation software *Thercast[®]*

CEMEF, as an academic partner, contributed to the work by proposing numerical models in view of predicting the chill cooling of steel droplets. A first model was developed by Rivaux [2011] whereas the present discusses a new model. The experimental work considered various facilities and environments to set a droplet of molten alloy in levitation: EML (fig. 1.8) for ground-based experiments, microgravity in parabolic flight or sounding rockets and last, microgravity condition on-board the International Space Station (ISS)

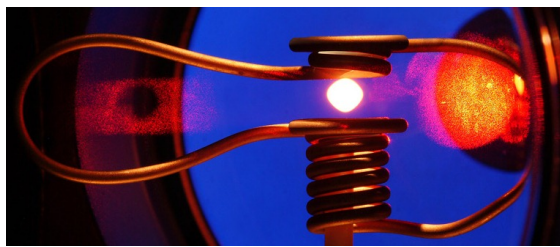


Fig. 1.8 – Electromagnetic levitation

1.4.2 Objectives and outline

The main focus of the present thesis is macrosegregation with liquid dynamics assuming a fixed solid phase, i.e. no account of solid transport (e.g. equiaxed crystals sedimentation) and no account of solid deformation. In CEMEF, this scope has been adopted for previous work by Gouttebroze [2005], Liu [2005], Mosbah [2008], Rivaux [2011], and Carozzani [2012]. Nevertheless, many modelling features evolved with time such as going from two-dimensional to three-dimensional modelling, resolution schemes for each of the conservation equations: energy, chemical species and liquid momentum, Eulerian or Lagrangian descriptions, modelling of grain structure and others. In this thesis, we propose a numerical model that takes into account i) the energy conservation in a temperature formulation based on a thermodynamic database mapping, ii) the liquid momentum conservation with thermosolutal convection and solidification shrinkage as driving forces, iii) solute mass conservation and iv) solidification paths at full equilibrium for multicomponent alloys microsegregation. Moreover, all equations are formulated in a pure Eulerian description while using the Level Set method to keep implicitly track of the interface between the alloy and surrounding gas. To the author's knowledge, this work combining macrosegregation prediction using the level set methodology to track the metal-air interface during shrinkage has no precedent in the literature.

Numerical tools: Cimlib relying on PETSc, parallelized with MPICH2, paraview and python as tools for postprocess and analysis.

The previously mentionned simulation requirements are not met in a single casting software package. Nevertheless, Thercast[®] is a promising tool that already handles a part of the above

Chapter 1. General Introduction

points. The current thesis developments are done using C++ language as a part of the in-house code, known as CimLib [Digonnet et al. 2007; Mesri et al. 2009]. This fully parallel library is the main academic research support for Thercast®.

Outline Each chapter content

Biblio test

Carozzani et al. [2013] is textual
[Carozzani et al. 2013] is parenthetical

Cross reference test

ref gives [1.2a](#)
cref gives [eq. \(1.2a\)](#)
Cref gives [Equation \(1.2a\)](#)
autoref gives [Equation 1.2a](#)

ref gives [1.3a](#)
cref gives [fig. 1.3a](#)
Cref gives [Figure 1.3a](#)
autoref gives [Figure 1.3a](#)

Chapter 2

Modelling Review

Contents

2.1 Modelling macrosegregation	12
2.1.1 Dendritic growth	12
2.1.2 Mush permeability	13
2.1.3 Microsegregation	13
2.1.4 Macroscopic solidification model: monodomain	16
2.2 Eulerian and Lagrangian motion description	18
2.2.1 Overview	18
2.2.2 Interface capturing	19
2.3 Solidification models with level set	19
2.4 The level set method	20
2.4.1 Transport and reinilaztion	20
2.4.2 Interface Remeshing	20
2.4.3 Mixing Laws	20

2.1 Modelling macrosegregation

2.1.1 Dendritic growth

In a casting process, the chill surface i.e. the contact between the molten alloy and relatively cold moulds, is the first area to solidify. Thermal gradient, G , and cooling rate R are two crucial process parameters that define the interface speed \vec{v}^* , which in turn, affects the initial microstructure. Although it may be not easy to control them, it remains important to understand their implication in solidification.

The solid-liquid interface fluctuates when solidifying, thus perturbations may appear on the front, locally destabilizing it. Two outcome scenarios are possible. The first scenario is characterized by low values of \vec{v}^* where the interface maintains a planar shape, hence we speak of *planar growth*. With this kind of growth, a random protuberance appearing at the interface, has a low tip velocity (low driving force of solidification). As such, the rest of the interface catches up, keeping the planar geometry. In another scenario, where a real casting is considered, the interface speed is greater in general, due to high solidification rate. The protuberance tip will be pulled into a liquid less rich in solute than the interface. The zone ahead of the solid-liquid interface is constitutionally undercooled [Tiller et al. 1953], giving a greater driving force for the protuberance to grow in the direction of the thermal gradient. As it has a tree-like shape, we speak of *dendritic growth*. Near the chill surface, dendrites are columnar, with a favourable growth in the $<100>$ direction for alloys with cubic lattices, but different orientations are also reported in the literature [see Dantzig et al. 2009, p. 289]. If temperature is uniform, which the case usually far from mould walls, a similar dendritic growth phenomenon occurs, but with an equiaxed morphology.

Columnar dendrites are characterized by a primary spacing, λ_1 , between the main trunks, and a secondary spacing, λ_2 , for the arms that are perpendicular to the trunks. It should be noted that λ_2 , together with the grain size, are two important microstructural parameters in the as-cast microstructure [Easton et al. 2011]. Further branching may occur but will not be discussed here.

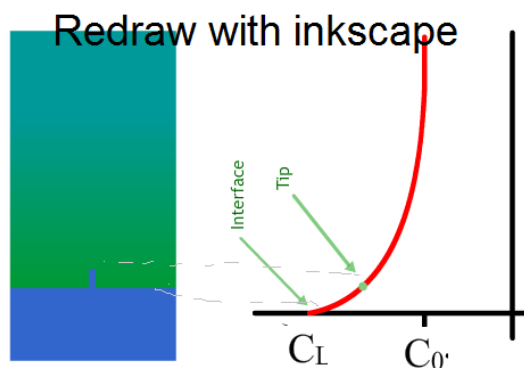


Fig. 2.1 – Schematic of a) a protuberance growing on the solid-liquid interface with b) the corresponding composition profiles (Reproduced and adapted from DoITPoMS [2000], © DoITPoMS, University of Cambridge)

2.1.2 Mush permeability

The dendritic geometry is crucial in solidification theory as it exhibits lower solid fraction compared to a microstructure formed by planar growth. This fact has consequences in the fluid-structure interaction in the mushy zone, namely the liquid flow through dendrites. At the chill surface, the solid grows gradually from dispersed growing nuclei, to a permeable solid skeleton until finally grains have fully grown with the end of phase change. The intermediate state where liquid can flow in and out of the mushy zone through the dendrites is a key phenomenon from a rheological perspective. The flow through the solid skeleton is damped by primary and secondary dendrites, resulting in momentum dissipation just like in saturated porous media. The famous [Darcy \[1856\]](#) law relates the pressure gradient ($\vec{\nabla} p$) to the fluid velocity \vec{v} , through the following equation [\[Rappaz et al. 2003\]](#):

$$\vec{v} = \frac{\mathbb{K}}{\mu} \vec{\nabla} p \quad (2.1)$$

where μ is the liquid dynamic viscosity and \mathbb{K} is the permeability tensor. The latter parameter has been the subject of numerous studies that aimed to predict it from various microstructural or morphological parameters. Some of these studies has started even before the first attempts to model macrosegregation by [Flemings et al. \[1967\]](#), [Flemings et al. \[1968a\]](#), and [Flemings et al. \[1968b\]](#). Basically, all models include the solid fraction, g^s , as input to predict mush permeability along with empirical data. An instance of such models is the work of [Xu et al. \[1991\]](#). Some models rely additionally on the primary dendrite arm spacing λ_1 like Blake-Kozeny [\[Ramirez et al. 2003\]](#), or the secondary dendrite arm spacing λ_2 like Carman-Kozeny, as a meaningful parameter to determine an isotropic permeability. Other models like [Poirier \[1987\]](#) and [Felicelli et al. \[1991\]](#) derive an anisotropic permeability based on both λ_1 and λ_2 . The present work uses Carman-Kozeny as a constitutive model for the permeability scalar (zero order tensor):

$$\mathbb{K} = \frac{\lambda_2^2 g^{l^3}}{180(1-g^l)^2} \quad (2.2)$$

2.1.3 Microsegregation

Microsegregation is a fundamental phenomenon in solidification. The simplest definition would be an uneven distribution of solute between liquid and the herein growing solid, at the microscopic scale of the interface separating these phases. If we consider a binary alloy, then the solubility limit is the key factor that dictates the composition at which a primary solid phase exists in equilibrium. The segregation (or partition) coefficient k determines the extent of solute rejection into the liquid during solidification:

$$k = \frac{w^{s^*}}{w^{l^*}} \quad (2.3)$$

where w^{s*} and w^{l*} are the compositions of the solid and liquid respectively, at the interface. When the segregation coefficient is less than unity (such is the case for most alloys during dendritic solidification), the first solid forms with a composition $kw^{l*} = kw_0$ less than the liquid's composition w_0 , the latter being initially at the nominal composition, w_0 . Figure 2.2 illustrates a typical binary phase diagram where the real solidus and liquidus are represented by solid lines, while the corresponding linear approximations are in dashed lines. For most binary alloys, this linearisation simplifies derivation of microsegregation models, as k becomes independent of temperature.

For each phase, the relationship between the composition at the interface and that in the bulk depends on the chemical homogenisation ability of the phase. The more homogeneous a phase, the closer the concentrations between the interface and the bulk, hence closer to equilibrium. It is thus essential to study the effect of homogenisation on the segregation behaviour and the subsequent effect on solidification, which leads the formalism of microsegregation models.

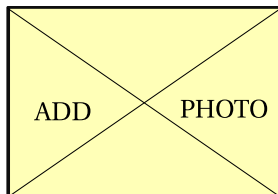


Fig. 2.2 – Simplified binary phase diagram

Microsegregation models

Solid formation depends greatly on the ability of chemicals species to diffuse within each of the solid and liquid phases, but also across the solid-liquid interface. Furthermore, chemical diffusion like all other diffusional process, is a time-dependent phenomenon. One can thus conclude that two factors influence the amount of solid formation: cooling rate and diffusion coefficients. However, convection and other mechanical mixing sources, homogenise the composition much faster than atomic diffusion. As such, *complete mixing* in the liquid is always an acceptable assumption, regardless of the solidification time. We may speak of infinite diffusion in the liquid. Nevertheless, diffusion in the solid also known as *back diffusion*, is the only transport mechanism with very low diffusion coefficients. Therefore, chemical species require a long time, i.e. low cooling rate, to completely diffuse within the solid. The difference in diffusional behaviour is summarized by two limiting segregation models of perfect equilibrium and nonequilibrium at the scale of a secondary dendrite arm, which are the lever rule and Gulliver-Scheil models, respectively. Afterwards, models with finite back diffusion are presented.

Lever rule

The lever rule considers an ideal equilibrium in all phases, i.e. solidification is extremely slow, hence phase compositions are homogeneous ($w^{l^*} = w^l$ and $w^{s^*} = w^s$) at all times as a consequence of complete mixing. These compositions are given by:

$$w^l = w^{l^*} = kw^{s^*} = kw^s \quad (2.4)$$

$$w^s = w^{s^*} = \frac{w_0}{k(1 - f^s) + f^s} \quad (2.5)$$

At the end of solidification, the composition of the solid phase is equal to the nominal composition, $w^s = w_0$

Gulliver-Scheil

The other limiting case is the absence of diffusion in the solid. That includes also the diffusion at the interface, so nothing diffuses in or out. The consequence is a steady increase of the homogeneous liquid composition while the solid composition remains non-uniform. Compared to a full equilibrium approach, higher fractions of liquid will remain until eutectic composition is reached, triggering a eutectic solidification. The phase compositions are given by:

$$w^l = w^{l^*} = kw^{s^*} \quad (2.6)$$

$$w^s = kw_0(1 - f^s)^{1-k} \quad (2.7)$$

Finite back diffusion

It has been concluded that the assumption of a negligible back diffusion overestimates the liquid composition and the resulting eutectic fraction. Therefore, many models studied the limited diffusion in the solid. One of the earliest models is the Brody-Flemings models [Khan et al. 2014] that is based on a differential solute balance equation for a parabolic growth rate, as follows:

$$w^l = w^{l^*} = kw^{s^*} \quad (2.8)$$

$$w^s = kw_0 \left[1 - \left(1 - 2\text{Fo}^s k \right) f^s \right]^{\frac{k-1}{1-2\text{Fo}^s k}} \quad (2.9)$$

where Fo^s is the dimensionless *Fourier number* for diffusion in the solid [Dantzig et al. 2009]. It depends on the solid diffusion coefficient D^s , solidification time t_s and the secondary dendrite arm spacing, as follows:

$$\text{Fo}^s = \frac{D^s t_s}{(\lambda_2/2)^2} \quad (2.10)$$

Several other models were since suggested and used. The interested reader is referred to the following non exhaustive list of publications: Clyne et al. [1981], Kobayashi [1988], Ni et al.

[1991], Wang et al. [1993], Combeau et al. [1996], Martorano et al. [2003], and Tourret et al. [2009].

2.1.4 Macroscopic solidification model: monodomain

In this section, we will present the macroscopic conservations equations that enable us to predict macrosegregation in the metal when the latter is the only domain in the system.

Volume averaging

It is crucial for a solidification model to represent phenomena on the microscale, then scale up to predict macrscopic phenomena. Nevertheless, the characteristic length of a small scale in solidification may represent a dendrite arm spacing, for instance the mushy zone permeability, as it may also represent an atomic distance if one is interested, for instance, in the growth competition between diffusion and surface energy of the solid-liquid interface. Modelling infinitely small-scale phenomena could be prohibitively expensive in computation time, if the we target industrial scales.

The volume averaging is a technique that allows bypassing this barrier by averaging small-scale variations on a so-called *representative volume element* (RVE) [Dantzig et al. 2009] with the following dimensional constraints on its volume, V_E : the element should be large enough to "see" and average microscopic fluctuations whilst being smaller than the scale of macroscopic variations. Solid and liquid may exist simultaneously in the RVE, but no gas phase is considered (volume saturation: $V^s + V^l = V_E$). Moreover, temperature is assumed uniform and equal for all the phases. The formalism, introduced by Ni et al. [1991], is summarized by the following equations for any physical quantity ψ :

$$\langle \psi \rangle = \frac{1}{V_E} \int_{V_E} \psi d\Omega = \langle \psi^s \rangle + \langle \psi^l \rangle \quad (2.11)$$

where $\langle \psi \rangle^s$ and $\langle \psi \rangle^l$ are phase averages of ψ . Then, for any phase ϕ , one can introduce the *phase intrinsic average* of ψ , denoted $\langle \psi \rangle^\phi$, by writing:

$$\langle \psi^\phi \rangle = \frac{1}{V_E} \int_{V^\phi} \psi d\Omega = g^\phi \langle \psi \rangle^\phi \quad (2.12)$$

where g^ϕ is the volume fraction of the phase. To finalize, the averaging is applied to temporal and spatial derivation operators [Rivaux 2011]:

$$\langle \frac{\partial \psi^\phi}{\partial t} \rangle = \frac{\partial \langle \psi^\phi \rangle}{\partial t} - \int_{\Gamma^*} \psi^\phi \vec{v}^* \cdot \vec{n}^\phi d\Gamma \quad (2.13)$$

$$\langle \vec{\nabla} \psi^\phi \rangle = \vec{\nabla} \langle \psi^\phi \rangle + \int_{\Gamma^*} \psi^\phi \vec{n}^\phi d\Gamma \quad (2.14)$$

where \vec{v}^* is the local relative interface velocity and Γ^* is the solid-liquid interface, while \vec{n}^ϕ is the normal to Γ^* , directed outwards. The surface integral term in eqs. (2.13) and (2.14) is an *interfacial average* that expresses interfacial exchanges between the phases. The previous

equations will be used to derive a set macroscopic conservation equations. It is noted that the intrinsic average $\langle \psi \rangle^\phi$ may be replaced by ψ^ϕ for notation simplicity, whenever the averaging technique applies.

Macroscopic equations

A monodomain macroscopic model relies on four main conservation equations to predict macrosegregation in a single alloy domain, i.e. the latter is considered without any interaction with another alloy or ambient air. The general form of a conservation equation of any physical quantity ψ is given by [Rappaz et al. 2003]:

$$\frac{\partial \psi}{\partial t} + \nabla \cdot (\psi \vec{v}) - \nabla \cdot \vec{j}_\psi = Q_\psi \quad (2.15)$$

The first LHS term in eq. (2.15) represents the time variation of ψ , the second term accounts for transport by advection while the third is the diffusive transport and the RHS term represents a volume source. The considered equations are mass, energy, liquid momentum and species conservation, all summarized in table 2.1. The solid momentum is not considered as we assume a fixed and rigid solid phase ($\vec{v}^s = \vec{0}$). We develop the ingredients of these equations

Table 2.1 – Summary of conservation equations with their variables

Conservation Equation	ψ	\vec{j}_ψ	Q_ψ
Mass	$\langle \rho \rangle$	–	–
Energy	$\langle \rho h \rangle$	$\langle \vec{q} \rangle$	–
Species	$\langle \rho w_i \rangle$	$\langle \vec{j}_i \rangle$	–
Liquid momentum	$\langle \rho \vec{v}^l \rangle$	$-\overline{\overline{\sigma^l}} \rangle$	\vec{F}_v^l

using the averaging technique, as follows:

$$\langle \rho \rangle = g^l \rho^l + g^s \rho^s \quad (2.16)$$

$$\langle \rho \vec{v} \rangle = g^l \rho^l \vec{v}^l + g^s \rho^s \vec{v}^s \quad (2.17)$$

$$\langle \rho h \rangle = g^l \rho^l h^l + g^s \rho^s h^s \quad (2.18)$$

$$\langle \rho h \vec{v} \rangle = g^l \rho^l h^l \vec{v}^l + g^s \rho^s h^s \vec{v}^s \quad (2.19)$$

$$\langle \rho w_i \rangle = g^l \rho^l w_i^l + g^s \rho^s w_i^s \quad (2.20)$$

$$\langle \rho w_i \vec{v} \rangle = g^l \rho^l w_i^l \vec{v}^l + g^s \rho^s w_i^s \vec{v}^s \quad (2.21)$$

Next we define the average diffusive fluxes, \vec{q} for energy and \vec{j}_i for solutes, using Fourier's conduction law and Fick's first law respectively:

$$\langle \vec{q} \rangle = -g^l \langle \kappa^l \rangle \vec{\nabla} T - g^s \langle \kappa^s \rangle \vec{\nabla} T \quad (2.22)$$

$$\langle \vec{j}_i \rangle = -g^l D^l \vec{\nabla} w_i^l - g^s D^s \vec{\nabla} w_i^s \quad (2.23)$$

In eq. (2.23), the solid diffusion coefficient is neglected, by considering that for macroscopic scales, the average composition of the alloy is much more influenced by advective and diffusive transport in the liquid.

Macro models:

- Rivaux ?
- Gu beckermann 1999 ?

MICRO MACRO:

- Tommy Carozzani (direct)
- P. Thévoz, J.-L. Desbiolles, M. Rappaz, Metallurgical and Materials TransactionsA 20 (2) (1989) 311–322
- guo beckermann 2003
- Combeau 2009
- Miha Zaloznik 2010 (indirect)

end by talking about taking air into account and the need for an interface capturing method

2.2 Eulerian and Lagrangian motion description

2.2.1 Overview

In mechanics, it is possible to describe motion using two well-known motion description: Eulerian and Lagrangian descriptions. To start with the latter, it describes the motion of a particle by attributing a reference frame that moves with the particle. In other words, the particle itself is the center of a reference frame moving at the same speed during time. As such, the total variation of any physical quantity ψ related to the particle can be found by deriving with respect to time:

$$\frac{d\psi}{dt} = \frac{\partial\psi}{\partial t} \quad (2.24)$$

In contrast to the Lagrangian description, the Eulerian description considers a fixed reference frame and independent of the particle's trajectory. The total variation of ψ cannot be simply described by a temporal derivative, since the particle's velocity is not known to the reference frame, and thus the velocity effect, namely the advective transport of ψ should also be considered as follows:

$$\frac{d\psi}{dt} = \frac{\partial\psi}{\partial t} + \underbrace{\vec{v} \cdot \vec{\nabla}\psi}_{\text{Advection Transport}} \quad (2.25)$$

In this case, the LHS term is also known as *total* or *material derivative*. The importance of these motion descriptions is essential to solve mechanics, whether for fluids or solids, using a numerical method like the finite element method (FEM). One of the main steps of this method is to spatially discretise a continuum into a grid of points (nodes, vertices ...), where any physical field shall be accordingly discretized. Now, if we focus on a node where velocity has a non zero value and following the previously made analysis, two outcomes are possible: either the node would be fixed (Eulerian) or it would move by a distance proportional to the prescribed velocity (Lagrangian). As a consequence, points located on the boundaries constantly require an update of the imposed boundary conditions.

From these explanations, one can deduce that an Eulerian framework is suited for fluid mechanics problems where velocities are high and may distort the mesh points, whereas the Lagrangian framework is better suited for solid mechanics problems where deformation velocities are relatively low and should well behave when predicting strains.

Another motion description has emerged some decades ago, [Hirt \[1971\]](#) call it the Arbitrary Langrangian-Eulerian (ALE) method. ALE combines advantages from both previous descriptions as it dictates a Lagrangian behavior at "solid" nodes where solid is deforming, and an Eulerian behavior at "fluid" nodes.

2.2.2 Interface capturing

As no solid deformation is considered in this work, the Eulerian framework is a convenient choice. Although solidification shrinkage is to be considered in the current scope, it will deform the alloy's outer surface in contact with the air. We intend to track this interface and its motion over time via a numerical method. A wide variety of methods accomplish this task while they yield different advantages and disadvantages. Such methods fall under two main categories, either interface tracking or interface capturing, among which we cite: marker-and-cell (MAC) [[Harlow et al. 1965](#)], volume of fluid (VOF) [[Hirt et al. 1981](#)], phase field methods (PF), level set method (LSM) [[Osher et al. 1988](#)], coupled level set - VOF method and others. The interested reader may refer to a quick reference by [Maitre \[2006\]](#) about these methods. In the past years, the level set method received a considerable attention in many computational fields, specifically in solidification. For this reason, we will focus on this method henceforth, giving a brief literature review and technical details in the next sections.

2.3 Solidification models with level set

In classic solidification problems, the need to track an interface occurs usually at the solid-liquid interface, that is why the phase field method [[Karma et al. 1996; Boettinger et al. 2002](#)] and the level set method [[Chen et al. 1997; Gibou et al. 2003; Tan et al. 2007](#)] were applied at a microscale to follow mainly the dendritic growth of a single crystal in an undercooled melt. In our case however, when we mention "solidification models using LSM", we do not mean the solid-liquid interface inside the alloy, but it is the alloy(liquid)-air interface that is tracked, assuming that microscale phenomena between the phases within the alloy, are

averaged using the previously defined technique in [section 2.1.4](#).

Very few models were found in the literature, combining solidification and level set as stated previously. [Du et al. \[2001\]](#) applied it to track the interface between two molten alloys in a double casting technique. In welding research, on another hand, has been more active adapting the level set methodology to corresponding applications. In Cemef, two projects were already based on the metal-air level set in welding simulations and showed promising results. Firstly, [Desmaison et al. \[2014\]](#)Later, [Chen \[2014\]](#) applied to gas metal arc welding (GMAW) to predict the grain structure in the heat affected zone essentially. More recently, in a related context, [Courtois et al. \[2014\]](#) used the same methodology but this time to predict keyhole defect formation in spot laser welding. The tracked interface in this case was that between the molten alloy and the corresponding vapor phase.

2.4 The level set method

How it is defined, Heaviside, mixing laws, transport and reinitialization

in the article 2004SunBeckermann, in the introduction there is a small discussion about the importance of the diffuse interface thickness, check references 3 and 10

2.4.1 Transport and reinitialization

Strong and weak form of transport

Numerical stability

Convective reinitialization and Hamilton-Jacobi equations

Geometric reinitialization

2.4.2 Interface Remeshing

Importance when using a static level set and more importantly when LS is transported, influence of mixing area *thickness* and *resolution* (i.e. nb of nodes with the area), Isotropic or anisotropic ? the first is more important to composition calculation while the second is more relevant if we mean do thermohydraulics without macrosegregation

2.4.3 Mixing Laws

Chapter 3

Energy balance with thermodynamic tabulations

Contents

3.1 State of the art	22
3.2 Thermodynamic considerations	22
3.2.1 Volume averaging	22
3.2.2 The temperature-enthalpy relationship	23
3.2.3 Tabulation of properties	23
3.3 Formulation	25
3.4 Validation	25
3.4.1 Pure diffusion	25
3.4.2 Convection-diffusion with macrosegregation	25

TODO: replace wt pct by the macro bin or tern

TODO: correct equations references prefix after replacing autoref by eqref

When we speak about macrosegregation in solidification, we have to remember that the problem is one that involves phase change.

3.1 State of the art

- Use of enthalpy resolution in the majority of works
- motivation and advantages of TvsH without talking about resolution time
- use article's introduction to fill this section (or improvise new things)

3.2 Thermodynamic considerations

this section should be revised for missing symbols, equations and figures from the corresponding article

3.2.1 Volume averaging

the following paragraph will be deleted once the volume averaging has been introduced in chapter 1

A volume averaging technique was suggested to deal with the presence of multiple phases [Ni et al. 1991]. It locally considers a Representative Volume Element (RVE) that contains a single or several phases (these are not necessarily in thermodynamic equilibrium) at a mesoscopic scale. We represent, for each unknown ψ , an intrinsic volume average, $\langle \psi \rangle^\phi$ (also denoted $\langle \psi^\phi \rangle^\phi$ in the literature), corresponding to a phase ϕ . The volume average $\langle \psi \rangle$ for this unknown in the RVE, hence averaged over all the present phases writes:

$$\langle \psi \rangle = \sum_{\phi} g^{\phi} \langle \psi \rangle^{\phi} \quad (3.1)$$

where g^{ϕ} denotes the volume fraction of phase ϕ in the RVE. It should be emphasized that the averaging technique applies to virtually all thermodynamic variables (enthalpy, density ...). Among these variables, the temperature is also considered to be uniform in the RVE. Applying the volume averaging technique to the energy conservation principle along with interfacial balances between the phases, results in the following averaged equation [Rappaz et al. 2003]:

$$\frac{\partial \langle \rho h \rangle}{\partial t} + \vec{\nabla} \cdot (\rho h \vec{v}) = \vec{\nabla} \cdot (\langle \kappa \rangle \vec{\nabla} T) + \langle \dot{Q}_V \rangle \quad (3.2)$$

where ρ stands for the density, h the mass enthalpy, \vec{v} the velocity field, κ the thermal conductivity, T the temperature and \dot{Q}_V a possible volume heat source. (3.2) is the standard averaged form of the energy conservation equation used in non-stationary phase change problems.

I could elaborate more in this paragraph by showing the possible equations for the explicit formulation and maybe a figure to show the AlSi7 computation that I did with a very small time step

Once the variational form has been discretized in space and time, two possible resolution schemes emerge: the first is an explicit forward Euler scheme which gives rise to a linear equation where the temperature is known at time t , T^t . This requires very small time steps in the current context, which limits the solver's usability at the scale of industrial applications. The second scheme is the backward Euler or full implicit discretization where terms are function of $T^{t+\Delta t}$. It leads to a nonlinear equation with 2 interdependent unknowns, $\langle \rho h \rangle^{t+\Delta t}$ and $T^{t+\Delta t}$. It is clear that the nature of the temperature-enthalpy relationship plays a central role when formulating the resolution strategy of this nonlinear equation. Generally, it is admitted that, depending on the resolution strategy, it is necessary to express enthalpy as a function of temperature or vice-versa, together with associated partial derivatives, $\frac{d\langle \rho h \rangle}{dT}$ or $\frac{dT}{d\langle \rho h \rangle}$.

3.2.2 The temperature-enthalpy relationship

In solidification problems, additional variables are involved in (3.1) and (3.2), like the transformation path that defines the history of the phase fractions, as well as the average chemical composition $\langle w_i \rangle$, i being the index of the chemical species (only the solutes are considered). The temperature-enthalpy relation averaged over the phases in a given RVE writes:

$$\langle \rho h \rangle = \sum_{\phi} g_{(T, \langle w_i \rangle, \dots)}^{\phi} \rho_{(T, \langle w_i \rangle^{\phi}, \dots)}^{\phi} h_{(T, \langle w_i \rangle^{\phi}, \dots)}^{\phi} \quad (3.3)$$

Note that the volume average enthalpy is approximated by the product $\langle \rho h \rangle^{\phi} = \langle \rho \rangle^{\phi} \langle h \rangle^{\phi}$ in the current work. As stated in the introduction, it becomes clear from (3.3) that phase properties, i.e. average phase density, ρ^{ϕ} and enthalpy, h^{ϕ} , are temperature and composition dependent. This equation is the key to convert the average volume enthalpy to temperature (through a procedure named H2T) or vice-versa (T2H). The values of the different phase fractions g^{ϕ} (solidification path) and phase enthalpies $\langle \rho h \rangle^{\phi}$ are thus needed to close the relation.

3.2.3 Tabulation of properties

The complexity of performing a thermodynamic conversion is directly linked to the simplicity of determining the alloy properties, namely the phase fractions and phase enthalpies. In the case of binary alloys and with several assumptions with respect to the system (e.g., linear monovariant temperature composition relationships, constant heat capacity of phases and constant latent heat of transformations, equilibrium approximations between phases) analytical calculations are often used to determine the properties. Nevertheless, analytical relations are more complex or even impossible to derive in the case of multicomponent alloys ($i > 1$). To overcome this problem, one can resort to thermodynamic databases and phase equilibrium calculations to tabulate the transformation paths and the phase enthalpies for a given range of temperatures and average compositions. It is a handy solution for two main

Chapter 3. Energy balance with thermodynamic tabulations

reasons: first, the conversion is merely a binary search in a table; secondly, it is a simple solution for coupling with macrosegregation. In this way, phase fractions g^ϕ are tabulated as functions of temperature and average composition, while for each phase ϕ the mass enthalpy, h^ϕ , and the density, ρ^ϕ , are tabulated as functions of temperature and phase intrinsic average compositions HERE, as well as other possible parameters. Figure 1 summarizes the steps in order to perform a temperature-to-enthalpy (T2H) conversion using the predefined tabulation approach. In step 1, the transformation path is acquired for each average composition and temperature to determine the list of phases, their volume fractions g^ϕ and their intrinsic compositions $\langle w_i \rangle^\phi$. In step 2, the phase enthalpy h^ϕ and density ρ^ϕ are determined by searching for the temperature and the already known phase composition $\langle w_i \rangle^\phi$. In step 3, the average volume enthalpy is computed from the volume fraction, density and mass enthalpy of phases using (3.3).

Figure 3 goes here

The methodology to build the tabulations is straightforward. It is based on two main scans. On the one hand, intervals for the variation of the average composition $\langle w_i \rangle$ are chosen from the known alloy composition. These variations have to cover the extreme values adopted during the simulation, which are not known a priori. An interval is also selected for the variation of temperature. The latter is easier to determine as it usually starts from the initial melt temperature and goes down to the room temperature in a standard casting simulation. For these intervals, a systematic scan is made with chosen steps in each composition and T, during which a thermodynamic equilibrium is computed. The outputs are the number of phases encountered, together with their fraction and intrinsic composition. The minimum and maximum intrinsic composition for each phase could then be determined. On the other hand, for each phase, a scan of the intrinsic composition and temperature is made to compute the intrinsic properties. The same temperature interval and step as defined earlier are used.

below paragraph should be re written and maybe stress LESS on the speed effect

I should change the superscript k which may be confused with partition coefficient

Regarding the enthalpy-to-temperature conversion (H2T), a backward iterative T2H search is performed. For a known composition $\langle w_i \rangle$, denoting k the iteration index to convert the enthalpy $\langle ph \rangle_{\text{input}}$, we start with an initial guess for temperature $T^{(k=0)}$ then convert it to an enthalpy $\langle ph \rangle^{(k=0)}$ with the T2H conversion. Using an appropriate nonlinear algorithm (Brent is the most versatile in our case), we aim at minimizing the following residual: $\text{Residu}_{\langle ph \rangle} = |\langle ph \rangle_{\text{input}} - \langle ph \rangle^{(k)}|$. Once the algorithm has converged, the temperature $T^{(k)}$ is the result of the H2T conversion. It is inferred that the first conversion (T2H) is a direct one whereas the latter (H2T) is indirect and requires a series of iterative steps; each step being a single T2H resolution. In other words, a H2T conversion is a backward search for a temperature, hence it's slower. This conversion's speed lag is exacerbated when tabulations increase in size (e.g. large number of temperature and composition steps) and complexity (e.g., multicomponent industrial alloys used in casting), since the search gets more complicated with the increasing number of input columns (one column for each alloying element).

3.3 Formulation

Coming soon

3.4 Validation

3.4.1 Pure diffusion

The two solvers are first tested in a purely diffusive case for a one-dimensional solidification configuration. Predictions with a 1D front tracking model [Gandin 2000] is used as a benchmark. It provides solutions for the temperature and solid fraction during directional solidification of a 10 cm long Al – 7 wt.% Si ingot. The melt, with initial uniform temperature, is cooled with a heat exchange coefficient (assuming a Fourier boundary condition) from one side, the other side being adiabatic. All values for alloy properties, initial and boundary conditions and numerical parameters are listed in [Table 3.1](#). For this simple test case, we use linear temperature dependence of the intrinsic phase enthalpies, that is $\langle \rho h \rangle^s = \langle \rho C_p \rangle T$ and $\langle \rho h \rangle^l = \langle \rho C_p \rangle T + \rho L$, where $\langle \rho C_p \rangle$ is the heat capacity per unit volume and ρL is the latent heat per unit volume. Values for $\langle \rho C_p \rangle$ and ρL , as well as for the thermal conductivities, $\kappa = \langle \kappa^l \rangle = \langle \kappa^s \rangle$, are taken constant. Moreover, a Gulliver Scheil approximation is used to compute a single temperature – fraction of solid relationship in the absence of macrosegregation. This is done assuming a linear binary phase diagram and thus requires using the properties listed in [Table 3.1](#), i.e. the segregation coefficient, k , the liquidus slope, m_L , the liquidus temperature, T_L , and the eutectic temperature, T_E . [Figure REF](#) shows the comparison with the Hsolver and Tsolver. The results are found superimposed to the front tracking solution, thus giving validation of the implementation as well as the iterative schemes presented above to solve the energy conservation.

3.4.2 Convection-diffusion with macrosegregation

Conservation equations in [Table 2](#) are for mass, momentum and chemical species. As for energy, they are presented after the volume averaging technique has been applied [Ni et al. 1991; Dantzig et al. 2009]. Moreover, an assumption of a static and non deformable solid phase is made. Consequently, the mechanical model is reduced to the conservation of momentum in the liquid phase. This assumption also yields some other consequences on the mass balance and the liquid momentum conservation. In the latter, a Darcy term is added to take into account the dissipative interfacial stress in the porous-like mushy zone. Its main parameter is the permeability of the mushy zone, K . It is considered isotropic, hence reducing to a scalar which is given by the Carman-Kozeny relation, based on the secondary dendrite arm spacing $\lambda_2 : K = \frac{g^{1/3} \lambda_2^2}{180(1-g^l)^2}$. The liquid density being taken constant, its spatial variations as a function of temperature and average composition are still needed to compute thermosolutal convection forces. For that purpose, the Boussinesq approximation $\langle \rho \rangle^l = \rho_{\text{ref}} (1 - \beta_T (T - T_{\text{ref}}) - \beta_{\langle w \rangle^l} (\langle w \rangle^l - w_{\text{ref}}^l))$ is used, considering the thermal β_T and solutal $\beta_{\langle w \rangle^l}$ expansion coefficients and a reference density, ρ_{ref} , defined at a reference temper-

Chapter 3. Energy balance with thermodynamic tabulations

Parameter	Symbol	Value	Unit
Nominal composition	$\langle w \rangle_0$	7	wt.%
Liquidus temperature	T_L	618	°C
Eutectic temperature	T_E	577	°C
Segregation coefficient	k	0.13	—
Liquidus slope	m_L	-6.5	K wt.% ⁻¹
Heat capacity (liquid and solid)	ρC_p	2.6×10^6	J m ⁻³ K ⁻¹
Enthalpy of fusion	ρL	9.5×10^8	J m ⁻³
Thermal conductivity (liquid and solid)	κ	70	W m ⁻¹ K ⁻¹
Heat transfer coefficient	h_{ext}	500	W m ⁻² K ⁻¹
External temperature	T_{ext}	100	°C
Initial temperature	T_0	800	°C
Ingot length		0.1	m
FE mesh size		10^{-3}	m
Time step	Δt	0.1	s
Convergence criterion (residual)	ε_R	10^{-6}	—
Convergence criterion (temperature)	ε_T	10^{-2}	K

Table 3.1 – Parameters for the pure diffusion test case with alloy Al – 7 wt.% Si presented in **FIGURE REF**

ature T_{ref} and reference composition w_{ref}^l . Values for the references are taken at the liquidus temperature and the nominal composition of the alloy, $\langle w \rangle_0$ [Carozzani et al. 2013]. More details about the FE formulation can be found in the Ph.D work of Rivaux [2011] and Carozzani [2012]. It should be noted that the macroscopic solute diffusion coefficient in the solid phase is neglected in **REF Eq. 15c**.

in this table I use directly the simplified equations, but this was done only for the article, now I have to go from the full conservation equations and state the hypothesis and methods that i used to reach this simplified form

$$\nabla \cdot (g^l \vec{v}^l) = 0 \quad (3.4a)$$

$$\frac{\partial}{\partial t} (g^l \rho_{\text{ref}} \vec{v}^l) + \vec{\nabla} \cdot (g^l \rho_{\text{ref}} \vec{v}^l \times \vec{v}^l) - \vec{\nabla} \cdot \langle S \rangle^l - g^l \nabla p^l + \mu^l g^{l2} K^{-1} \vec{v}^l - g^l \rho^l \vec{g} = 0 \quad (3.4b)$$

$$\frac{\partial}{\partial t} (\langle w_i \rangle) + (g^l \vec{v}^l) \cdot \vec{\nabla} w_i^l + \nabla \cdot (g^l D^l \vec{\nabla} w_i^l) = 0 \quad (3.4c)$$

Table 3.2 – Averaged conservation equations for the conservation of mass (a), momentum (b) and solute mass (c)

Figure SMACS: Computed unidirectional heat diffusion during solidification of an Al – 7 wt.% Si alloy using (orange) the enthalpy method and (black) the temperature method, comparison being made for (left) cooling curves and (right) time history of the liquid fraction. Each curve corresponds to a position along the sample, from 0 cm (cooling side) to 10 cm (insulated side), with 2 cm spacing between the positions.

The Tsolver's ability to be coupled with various physical phenomena like macrosegregation

and fluid flow in porous medium is displayed in this test case. It consists of a solidification benchmark where a 10 cm width \times 6 cm height \times 1 cm thick cavity containing a Sn – 3 wt.% Pb melt is cooled down from its two narrowest vertical sides using heat exchangers (LHE: left heat exchanger, RHE: right heat exchanger). The experiment, inspired by [Hebditch et al. \[1974\]](#) similar set up, has been revisited by [Hachani et al. \[2012\]](#) who performed the solidification with better controlled conditions and using an increased number of samples for composition analysis. Recently, a successful attempt to simulate the experiment was carried out by [Carozzani et al. \[2013\]](#) relying on an enthalpy resolution. All details regarding geometry, finite element discretization, material properties and boundary conditions can be found in [the latter reference](#).

I could develop more here giving additional details

For this computation, solidification paths, phase compositions and phase enthalpies were determined by a thermodynamic module dedicated to equilibrium calculations for binary alloys. The 3D simulation results in [REF Figure 4](#) show a satisfactory agreement with the experimental temperature measurements recorded at mid heights of the cavity and uniformly distributed along its width [[Carozzani et al. 2013](#)]. In fact, simulation results with the Tsolver and the Hsolver were found to be almost superimposed, as in [REF Figure 4](#). Regarding the computation, the Tsolver resolution proves to be faster than the Hsolver used by [Carozzani et al. \[2013\]](#): a process time of 7000s required a computation time of 90 hours 13 minutes compared to 114 hours 21 minutes spent by the enthalpy resolution with 32 cores on the same cluster. The gain factor is about 20%.

Chapter 4

Macrosegregation with incompressible fluid motion

Contents

4.1	Introduction	30
4.2	Review fluid mechanics	30
4.3	VMS solver	30
4.4	Computational stability	30
4.4.1	Integration order	30
4.5	Application to multicomponent alloys	31
4.5.1	Tabulations	31
4.6	Macroscopic freckle prediction	33
4.6.1	Introduction	33
4.6.2	Experimental work	33
4.6.3	Macroscopic scale simulations	33
4.7	Meso-Macro Freckle prediction	34

this chapter discusses the following points:

- Review fluid mechanics briefly (MINI element and VMS and talk about the available solvers in Cimlib)
- Give the VMS equations referring to Hachem article
- Coupling the energy resolution from chapter 2 to fluid mechanics and solute balance
- Make a transition to speak about freckles
- Application: Ternary solidification with freckles
- Application: Macroscopic Freckle prediction: pure FE
- Application Multi-scale Freckle prediction: FE + grain structure (in which lies a part about nucleation-growth and how numerically we reach a smaller scale, the scale of the grain boundaries)

4.1 Introduction

The previous chapter covered the energy solver ...

4.2 Review fluid mechanics

Review fluid mechanics briefly (MINI element and VMS and talk about the available solvers in Cimlib)

4.3 VMS solver

Give the VMS equations referring to Hachem article + weak form + stabilization

As for the last equation in [table 2.1](#), we follow the assumption of an incompressible liquid phase, which gives:

$$\frac{\partial \langle \rho \rangle}{\partial t} = 0 \quad (4.1)$$

4.4 Computational stability

CFL condition

4.4.1 Integration order

Using P1 linear elements implies a P2 integration ? what are the advantages (time) and limitations ?

4.5 Application to multicomponent alloys

This next section shows an application where Tsolver is used with incompressible fluid mechanics and solute conservation in a multicomponent configuration (this is the main difference from SMACS actually) we see freckles also during the analysis, this is the transition for the section after

The efficiency of the temperature-based resolution resides in its performance when combined with thermodynamic tabulations. A multicomponent alloy consists of at least two solute elements, and therefore the tabulation size increases, hence the number of search operations also increases. To demonstrate the speed-up ability of the temperature-based approach while predicting all phase transformations during macrosegregation, we consider the solidification of a ternary alloy, Fe–2 wt.%C–30 wt.%Cr. As illustrated in **Figure 5a**, the alloy domain has a cylinder shape close to 3-inch height × 1-inch diameter. Exact values are reported in **Table 3** with all material properties, initial and boundary conditions, as well as numerical parameters for the simulations. The melt steel is initially at 1395 °C. The temperature of the bottom surface is imposed with a constant decreasing rate of 0.1 K s⁻¹ starting with 1380 °C, i.e. 40 °C higher than the nominal liquidus temperature, as shown in **Figure 5b**. The other surfaces are kept adiabatic. The cylinder is held in a vertical position. In these conditions, and knowing that the carbon and chromium solutes have lightening effects on the liquid at nominal composition, the density inversion resulting from the composition gradient in the interdendritic liquid, may cause flow instability (segregation plumes) at the solidification front. While the selected alloy is a steel, this application is also representative of directional cooling in a single crystal casting, e.g. for nickel-base superalloys [Beckermann et al. 2000]. **Figure 5c** also provides the transformation path of the alloy at nominal composition, i.e. assuming no macrosegregation and full thermodynamic equilibrium as computed with ThermoCalc and the TCFE6 database. A total of 5 phases need to be handled, the characteristic temperature for their formation being reported in **Figure 5b**.

Figure 5: Configurations for directional casting of (a) a 1 inch diameter × 3 inches height cylindrical domain for which (b) temperature-time conditions are imposed at its bottom surface. The alloy is Fe – 2 wt.% C– 30 wt.% Cr, its computed transformation path at nominal composition being displayed in (c)

4.5.1 Tabulations

Full thermodynamic equilibrium is considered in the present case. Due to macrosegregation, the average composition is expected to continuously vary in time and space during casting. Transformation paths are thus determined a priori for a set of average compositions around the nominal value. Hence, carbon content is arbitrarily varied in the interval [1.8 wt.%, 2.2 wt.%] while chromium content variation is in the interval [27 wt.%, 33 wt.%]. The offset of ±10% with respect to the nominal composition value allows tabulating relatively small composition steps to ensure a good accuracy when compared to the corresponding ternary phase diagram. The average composition step is -0.04wt.% for carbon and -0.6wt.% for chromium, thus representing 2% intervals with respect to the nominal composition. The temperature varies in the interval [100 °C, 1600 °C] by 5 °C steps. For each triplet (carbon content in wt.% C,

Chapter 4. Macrosegregation with incompressible fluid motion

HERE , chromium content in wt.% Cr, HERE, temperature in K) corresponds a phase fraction g^ϕ and a pair of intrinsic phase composition (HERE). For the 5 phases listed in **Figure 5c** (LIQ≡liquid, BCC≡ferrite, FCC≡austenite, M₇C₃ ≡carbide, CEM≡cementite), the enthalpy h^ϕ and density ρ^ϕ , are tabulated as functions of temperature and phase intrinsic composition. If this latter input lies between two tabulated values, a linear interpolation is performed to determine the output, i.e. phase enthalpy and density. With the advancement of solidification, the liquid is enriched with solute by macrosegregation, which enables new solidification paths. It means that the primary solidifying phase is not necessarily the same as when considering the nominal composition. For this reason, the tabulation approach is interesting inasmuch as it provides phase transformation paths and values of phase properties that are compatible with the system's actual composition. **Figure 6** summarizes the tabulated thermodynamic data for two sets of average composition for the considered ternary system. Note that in the present test case, phase densities are taken constant ($\rho^s = \rho^l = 6725 \text{ kg m}^{-3}$). Therefore they are not tabulated. With this assumption, no shrinkage occurs upon phase change.

Table 4.1 – Parameters for solidification of alloy Fe – 2 wt.% C – 30 wt.% Cr

Parameter	Symbol	Value	Unit
Nominal composition	$\langle w_C \rangle_0$	2	wt.%
	$\langle w_{\text{Cr}} \rangle_0$	30	wt.%
Characteristic temperatures	$T_{\text{top}}, T_{\text{bottom}}$	FIGURE	°C
Phase fraction	g^ϕ	Tabulations	–
Phase enthalpy	$\langle h \rangle^\phi$	Tabulations	–
Phase composition	$\langle w_C \rangle^\phi$	Tabulations	wt.%
	$\langle w_{\text{Cr}} \rangle^\phi$	Tabulations	wt.%
Diffusion coefficients	$\langle D_C \rangle^l$	15×10^{-10}	$\text{m}^2 \text{s}^{-1}$
	$\langle D_{\text{Cr}} \rangle^l$	15×10^{-10}	$\text{m}^2 \text{s}^{-1}$
Dynamic viscosity	μ^l	2×10^{-3}	Pas
Thermal expansion coefficient	β_T	8.96×10^{-5}	K^{-1}
Solutal expansion coefficient	$\beta_{\langle w_C \rangle^l}$	1.54×10^{-3}	wt.\%^{-1}
	$\beta_{\langle w_{\text{Cr}} \rangle^l}$	1.72×10^{-2}	wt.\%^{-1}
Thermal conductivity in the solid	$\langle \kappa^s \rangle$	40	$\text{W m}^{-1} \text{K}^{-1}$
Thermal conductivity in the liquid	$\langle \kappa^l \rangle$	28	$\text{W m}^{-1} \text{K}^{-1}$
Dendrite arm spacing	λ	60×10^{-6}	m
Density	ρ_{ref}	6725	kg m^{-3}
Initial temperature	T_0	1395	°C
Ingot diameter		25×10^{-3}	m
Ingot length		75×10^{-3}	m
FE mesh size		10^{-3}	m
Time step	Δt	0.1	s
Convergence criterion (residual)	ε_R	10^{-6}	–
Convergence criterion (temperature)	ε_T	10^{-2}	K

4.6 Macroscopic freckle prediction

4.6.1 Introduction

I have shown the results of multicomponent alloy solidification, where we saw freckles. So let me do an introduction about freckles, the need to prevent such defect from forming (superalloys, critical use in turbine blades)

4.6.2 Experimental work

Then introduce the experimental benchmark of Natalia and Sven from the article to show that there's an effort to understand, characterize and prevent if possible freckle formation. Show figures and some experimental results but quickly, no need to put many things and distract the reader

4.6.3 Macroscopic scale simulations

Introduce the FE model and algorithm then show pure FE RESULTS

Discussion

In the literature, many successful attempts have been made to predict freckles since (for example CITE fellicelli, poireau) ... until coming to kohler thesis results in 2008. These authors tackled the problem from an qualitative perspective. To our knowledge, the only close-to-quantitative work in solidification literature was done by Ramirez et al. [2003], who attempted to draw a correlation (freckling criterion) between the process parameters and the occurrence of freckles, (without any size or shape constraints, i.e. any flow instability that may appear and form the smallest freckle is considered). To accomplish this, they took a number of experiments done independently by Pollock et al. [1996] and Auburtin et al. [2000] where the casting parameters vary one at a time: casting speed (R), thermal gradient (G), angle (θ) with respect to vertical orientation and nominal composition ($\langle w_0 \rangle$), giving a database for 6 different superalloys. The experimental results were compared to a modified Rayleigh number that accounts for the various parameters. It allowed them to define a threshold for freckle formation in Nickel-base superalloys, as well as Pb-Sn alloys.

They have also investigated Pb-Sn alloys, check

Other contributions by Yuan et al. [2012] and Karagadde et al. [2014] used a medium scale model to compare the simulated formation of freckles with the results obtained by Shevchenko et al. [2013] (explain at bit more) However, all simulations show common traits in their predictions: (some words about the freckle dimensions, shape, intensity). These properties do not exactly meet with the experimental observations, just like in the In-Ga experiment. We think that the hydrodynamics scale at which freckles are born, is much smaller than the FEM scale. Since the relevant physics are not solved, even the finest FE mesh will not be enough to see the exact grain boundaries. (now it is time to do transition to CAFE)

4.7 Meso-Macro Freckle prediction

parachute article :)

Chapter 5

Macrosegregation with solidification shrinkage

Contents

5.1	Literature review	36
5.2	Level set treatment	36
5.2.1	Permeability mixing	36
5.3	Conservation equations	37
5.3.1	Mass Conservation	37
5.3.2	Momentum Conservation	38
5.3.3	Energy Conservation	41
5.3.4	Species Conservation	43
5.4	Test cases	44
5.4.1	Validation of LS transport	44
5.4.2	Shrinkage without macrosegregation	44

this chapter discusses the following points:

- Density variation during solidification (industrial point of view then how to handle numerically)
- Model equations
- Application to solidification benchmark SMACS
- Possible extension of application with grain structure (using Shijia's LS-air cells handling)
- Multiscale Freckle prediction: FE + grain structure (in which lies a part about nucleation-growth and how numerically we reach a smaller scale, the scale of the grain boundaries)

5.1 Literature review

Solidification shrinkage is, by definition, the effect of relative density change between the liquid and solid phases. In general, it results in a progressive volume change during solidification, until the phase change has finished. The four stages in [figs. 5.1a](#) to [5.1d](#) depict the volume change with respect to solidification time. First, at the level of the first solid crust, near the local solidus temperature, the solid forms with a density smaller than the liquid's. This does not necessarily apply for all materials, but at least for steels it does. The subsequent volume difference tends to create voids with a big negative pressure, that needs to be compensated by a surrounding fluid. It thus drains the liquid metal in its direction (cf. [Figure 5.1b](#)). As a direct result of the inward feeding flow, the ingot surface tends to gradually deform in the feeding direction, forming the so-called *shrinkage pipe*. Since the mass of the alloy and its chemical species is conserved, a density difference between the phases ($\rho^l < \rho^s \implies \frac{\rho^l}{\rho^s} < 1$) eventually leads to a different overall volume ($V^s < V^l$) once solidification is complete, as confirm the following equations:

$$\rho^l V^l = \rho^s V^s \quad (5.1a)$$

$$V^s = \frac{\rho^l}{\rho^s} V^l \quad (5.1b)$$

Sutaria2012 talk about feeding paths, but more importantly they computed thermal shrinkage WITHOUT solving NavierStokes equations. To predict the interface shape, they solve a LS transport with an imposed velocity given by Gada et Sharma 2009

5.2 Level set treatment

5.2.1 Permeability mixing

How to mix liquid fraction, best using harmonic or arithmetic, in order to replicate the effect the of non slip condition at top for example

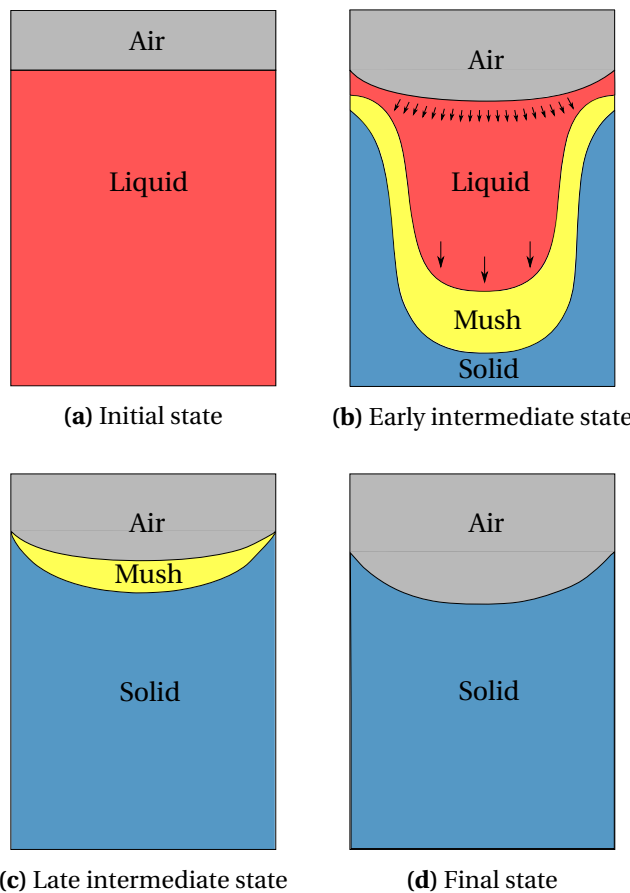


Fig. 5.1 – Schematic of the main cooling stages of an ingot against side and bottom mould walls (not shown)

Put the python plots from the presentations in "TEXUS monolithic"
Put video animations of PSEUDO SMACS 2D without and with LS ???

5.3 Conservation equations

5.3.1 Mass Conservation

Assumptions

- Two phases are considered, liquid l and solid s : $g^l + g^s = 1$
- The phase densities are constant but not equal: $\rho^l = cst_1$ and $\rho^s = cst_2$. Thermal and solutal expansion/contraction is neglected
- The solid phase is assumed static: $\vec{v}^s = \vec{0}$, which yields the following consequences:

$$\begin{aligned} 1. \quad \langle \vec{v} \rangle &= g^l \vec{v}^l + g^s \vec{v}^s = g^l \vec{v}^l \\ 2. \quad \langle \rho \vec{v} \rangle &= g^l \rho^l \vec{v}^l + g^s \rho^s \vec{v}^s = g^l \rho^l \vec{v}^l \end{aligned}$$

$$3. \vec{\nabla} \rho^l = \vec{\nabla} \rho^s = \vec{0}$$

Formulation

The mass balance equation averaged over the two phases, is expanded taking into account the aforementioned assumptions.

$$\frac{\partial \langle \rho \rangle}{\partial t} + \nabla \cdot \langle \rho \vec{v} \rangle = 0 \quad (5.2a)$$

$$\frac{\partial}{\partial t} (g^l \rho^l + g^s \rho^s) + \nabla \cdot (g^l \rho^l \vec{v}^l) = 0 \quad (5.2b)$$

$$g^l \frac{\partial \rho^l}{\partial t} + \rho^l \frac{\partial g^l}{\partial t} + g^s \frac{\partial \rho^s}{\partial t} + \rho^s \frac{\partial g^s}{\partial t} + \rho^l \nabla \cdot (g^l \vec{v}^l) + g^l \vec{v}^l \cdot \vec{\nabla} \rho^l = 0 \quad (5.2c)$$

$$(\rho^l - \rho^s) \frac{\partial g^l}{\partial t} + \rho^l \nabla \cdot (g^l \vec{v}^l) = 0 \quad (5.2d)$$

$$\nabla \cdot (g^l \vec{v}^l) = \nabla \cdot \langle \vec{v}^l \rangle = \frac{\rho^l - \rho^s}{\rho^l} \frac{\partial g^s}{\partial t}$$

(5.3)

Discussion

With the assumptions of static solid phase and constant unequal phase densities, the average mass balance states that the divergence of the liquid velocity is proportional to the solidification rate, the proportionality constant being the relative density change (which results in a relative volume change). This relation between the liquid velocity and the temporal derivative of the solid fraction, explains the flow due to shrinkage. In metallic alloys, the solid density is usually greater than the liquid density, therefore the first term in the RHS is negative. As for the second term, if we neglect remelting, then it'll be positive in the solidifying areas of the alloy. A negative divergence term in these areas, means that a liquid feeding is necessary to compensate for the density difference, hence acting as a flow driving force in the melt. In the case of constant densities, we can easily deduce that the divergence term is null, and therefore no flow is induced by solidification.

Numerically speaking, a non-zero divergence term in the mass balance is equivalent to a compressible fluid behaviour. Additional terms should appear in the other conservation equations, balancing the volume change in the momentum, heat and species transport.

5.3.2 Momentum Conservation

In a typical volume averaging approach, one would write one momentum conservation equation for each phase. Nonetheless, only one equation will be present in our case, and that is the consequence of the assumption of the static solid, made in the previous section. It should be emphasized that, despite considering a single conservation equation, the effect of the solid movement with respect to the liquid's can still be incorporated through the interfacial fluxes in the momentum conservation of the liquid phase.

Assumptions

- The interfacial momentum transfer between the solid and liquid phases is modelled by a momentum flux vector $\vec{\Gamma}^l$, consisting of hydrostatic and deviatoric parts, such that:

$$\vec{\Gamma}^l = \vec{\Gamma}_p^l + \vec{\Gamma}_{\mathbb{S}}^l \quad (5.4a)$$

$$\vec{\Gamma}_p^l = p^{l*} \vec{\nabla} g^l = p^l \vec{\nabla} g^l \quad (5.4b)$$

$$\vec{\Gamma}_{\mathbb{S}}^l = -g^{l2} \mu^l \mathbb{K}^{-1} (\vec{v}^l - \vec{\nu}) \quad (5.4c)$$

where p^{l*} is the pressure at the interface, considered to be equal to the liquid hydrostatic pressure, \mathbb{K} is the permeability computed by the Carman-Kozeny relation and μ^l is the liquid's dynamic viscosity. For the solid phase, the interfacial terms are the opposite, which cancels them out with the liquid terms if the phase momentum equations are summed up.

- The liquid is considered as a *compressible* Newtonian fluid. It implies that the deviatoric part, $\underline{\underline{\mathbb{S}}}^l$, of the Cauchy stress tensor is decomposed as follows:

CAG: the liquid is incompressible, but the mixture is compressible, change it

$$\langle \underline{\underline{\sigma}}^l \rangle = -\langle p^l \rangle \underline{\underline{I}} + \langle \underline{\underline{\mathbb{S}}}^l \rangle \quad (5.5a)$$

$$\langle \underline{\underline{\sigma}}^l \rangle = -\langle p^l \rangle \underline{\underline{I}} + 2\mu^l \langle \dot{\underline{\underline{\epsilon}}}^l \rangle + \langle \underline{\underline{\tau}}^l \rangle \quad (5.5b)$$

where $\langle \dot{\underline{\underline{\epsilon}}}^l \rangle$ is the strain rate tensor that depends on the average liquid velocity:

$$\langle \dot{\underline{\underline{\epsilon}}}^l \rangle = \bar{\nabla} \langle \vec{v}^l \rangle + \bar{\nabla}^t \langle \vec{v}^l \rangle \quad (5.6)$$

and $\underline{\underline{\tau}}^l$ is the extra stress tensor in the liquid, given by:

$$\langle \underline{\underline{\tau}}^l \rangle = -\lambda \nabla \cdot \langle \vec{v}^l \rangle \underline{\underline{I}} \quad (5.7a)$$

where λ is a dilatational viscosity **CITE RAP2003**. For an incompressible flow, the divergence term vanishes, hence the classical Newtonian constitutive law is retrieved. In the literature, the coefficient λ is taken proportional to the viscosity: $\lambda = \frac{2}{3} \mu^l$

Formulation

The momentum conservation equation in the liquid writes:

$$\frac{\partial}{\partial t} (\rho^l g^l \vec{v}^l) + \vec{\nabla} \cdot (\rho^l g^l \vec{v}^l \times \vec{v}^l) = \vec{\nabla} \cdot (g^l \underline{\underline{\sigma}}^l) + g^l \vec{F}_v + \vec{\Gamma}^l \quad (5.8)$$

Chapter 5. Macrosegregation with solidification shrinkage

where \vec{F}_v is an external volume force. The effect of the mass balance obtained in the previous section is incorporated by expanding the temporal and spatial derivatives in the momentum equation, taking firstly the left-hand side of equation (5.8).

$$\text{LHS} = \rho^l \frac{\partial}{\partial t} \left(g^l \vec{v}^l \right) + g^l \vec{v}^l \frac{\partial \rho^l}{\partial t} + \vec{v}^l \nabla \cdot \left(\rho^l g^l \vec{v}^l \right) + \bar{\nabla} \vec{v}^l \left(\rho^l g^l \vec{v}^l \right) \quad (5.9a)$$

$$= \underbrace{\rho^l \frac{\partial}{\partial t} \left(g^l \vec{v}^l \right)}_{\text{Unsteady Acceleration}} + \underbrace{\left(\rho^l - \rho^s \right) \frac{\partial g^s}{\partial t} \vec{v}^l}_{\text{Shrinkage Acceleration}} + \underbrace{\rho^l \bar{\nabla} \vec{v}^l \left(g^l \vec{v}^l \right)}_{\text{Advection Acceleration}} \quad (5.9b)$$

The development in (5.9b) shows that the origin of the flow, namely its acceleration, is attributed to three causes: i) unsteady acceleration: a temporal change of a particle's velocity, ii) shrinkage-induced acceleration: a local "suction" effect at the solid-liquid interface (where $\frac{\partial g^s}{\partial t} > 0$) caused by the density jump ($\rho^l - \rho^s$) and iii) convective acceleration: a spatial change in the velocity field. The effect of the *shrinkage-induced* flow is introduced using the mass balance in equation (5.3). The right-hand side of equation (5.8) is now expanded:

$$\text{RHS} = \bar{\nabla} \cdot \left(\langle p^l \rangle \bar{\mathbb{I}} + 2\mu^l \langle \dot{\bar{\varepsilon}}^l \rangle + \langle \bar{\tau}^l \rangle \right) + g^l \rho^l \vec{g} + \vec{\Gamma}_p^l + \vec{\Gamma}_{\mathbb{S}}^l \quad (5.10a)$$

$$= -\bar{\nabla} \left(g^l p^l \right) + \bar{\nabla} \cdot \left(2\mu^l \langle \dot{\bar{\varepsilon}}^l \rangle \right) + \bar{\nabla} \cdot \left(-\frac{2}{3} \mu^l \nabla \cdot \langle \vec{v}^l \rangle \bar{\mathbb{I}} \right) + g^l \rho^l \vec{g} + \vec{\Gamma}_p^l + \vec{\Gamma}_{\mathbb{S}}^l \quad (5.10b)$$

$$= -p^l \bar{\nabla} \vec{g}^T - g^l \bar{\nabla} p^l + \bar{\nabla} \cdot \left(2\mu^l \langle \dot{\bar{\varepsilon}}^l \rangle \right) + \bar{\nabla} \cdot \left(-\frac{2}{3} \mu^l \nabla \cdot \langle \vec{v}^l \rangle \bar{\mathbb{I}} \right) + g^l \rho^l \vec{g} + \vec{\Gamma}_p^l + \vec{\Gamma}_{\mathbb{S}}^l \quad (5.10c)$$

$$= -g^l \bar{\nabla} p^l + \bar{\nabla} \cdot \left(\mu^l \left(\bar{\nabla} \langle \vec{v}^l \rangle + \mathbf{t} \bar{\nabla} \langle \vec{v}^l \rangle \right) \right) + \bar{\nabla} \left(-\frac{2}{3} \mu^l \frac{\rho^l - \rho^s}{\rho^l} \frac{\partial g^s}{\partial t} \right) + g^l \rho^l \vec{g} - g^{l2} \mu^l \mathbb{K}^{-1} \vec{v}^l \quad (5.10d)$$

The system thus consists of 3 equations (one for each of the components of \vec{v}^l) and 4 unknowns (\vec{v}_x^l , \vec{v}_y^l , \vec{v}_z^l and p). An additional equation is provided by the mass continuity equation (5.3). For convenience, the superficial velocity $\langle \vec{v}^l \rangle$ will be chosen as a velocity unknown instead of the intrinsic average: $\langle \vec{v}^l \rangle = g^l \vec{v}^l$. The final system to solve, after grouping the unknowns in the LHS and the remaining terms in the RHS, is given by:

I changed *split* to *align* here

$$\rho^l \frac{\partial \langle \vec{v}^l \rangle}{\partial t} + \frac{\rho^l - \rho^s}{g^l} \frac{\partial g^s}{\partial t} \langle \vec{v}^l \rangle + \rho^l \bar{\nabla} \vec{v}^l \langle \vec{v}^l \rangle + \bar{\nabla} \cdot \left(2\mu^l \langle \dot{\bar{\varepsilon}}^l \rangle \right) + g^l \mu^l \mathbb{K}^{-1} \langle \vec{v}^l \rangle \quad (5.11)$$

$$= g^l \bar{\nabla} p^l + \bar{\nabla} \left(-\frac{2}{3} \mu^l \nabla \cdot \langle \vec{v}^l \rangle \right) + g^l \rho^l \vec{g} \quad (5.12)$$

$$\nabla \cdot \langle \vec{v}^l \rangle = \frac{\rho^l - \rho^s}{\rho^l} \frac{\partial g^s}{\partial t} \quad (5.13)$$

5.3.3 Energy Conservation

We have seen the averaged energy conservation equation in the case of two phases: a solid phase and an incompressible liquid phase. However, with the incorporation of the shrinkage effect, new terms should appear in the advective-diffusive heat transfer equation.

Assumptions

- The thermal conductivity is constant for both phases: $\langle \kappa \rangle = \langle \kappa^s \rangle = \langle \kappa^l \rangle = \kappa$
- Consequence of the static solid phase: $\langle \rho h \vec{v} \rangle = g^l \rho^l h^l \vec{v}^l + g^s \rho^s h^s \vec{v}^s = g^l \rho^l h^l \vec{v}^l$
- The system's enthalpy may thermodynamically evolve with pressure, knowing that $h = e + \frac{p}{\rho}$, where e is the internal energy and p is the pressure. It infers that the heat transport equation may contain a contribution attributed to volume compression/expansion:

$$\frac{\partial p}{\partial t} + \nabla \cdot (p \vec{v}) = \frac{\partial p}{\partial t} + p \nabla \cdot \vec{v} + \vec{v} \cdot \vec{\nabla} p \quad (5.14)$$

In the literature, this contribution has been always neglected, even when accounting for solidification shrinkage, owing to the small variations of pressure.

- Another contribution is also neglected in solidification problems, that is the heat generated by mechanical deformation, $\mathbb{S} : \dot{\epsilon}$

Formulation

The unknowns in the energy conservation are the average volumetric enthalpy $\langle \rho h \rangle$ and temperature T . The energy conservation equation writes:

$$\frac{\partial \langle \rho h \rangle}{\partial t} + \nabla \cdot (\langle \rho h \vec{v} \rangle) = \nabla \cdot (\langle \kappa \rangle \vec{\nabla} T) \quad (5.15a)$$

$$\frac{\partial \langle \rho h \rangle}{\partial t} + \nabla \cdot (g^l \rho^l h^l \vec{v}^l) = \nabla \cdot (\kappa \vec{\nabla} T) \quad (5.15b)$$

$$\frac{\partial \langle \rho h \rangle}{\partial t} + \rho^l h^l \nabla \cdot \langle \vec{v}^l \rangle + \langle \vec{v}^l \rangle \cdot \vec{\nabla} (\rho^l h^l) = \nabla \cdot (\kappa \vec{\nabla} T) \quad (5.15c)$$

$$\frac{\partial \langle \rho h \rangle}{\partial t} + \rho^l h^l \frac{\rho^l - \rho^s}{\rho^l} \frac{\partial g^s}{\partial t} + \langle \vec{v}^l \rangle \cdot \vec{\nabla} (\rho^l h^l) = \nabla \cdot (\kappa \vec{\nabla} T) \quad (5.15d)$$

$$\frac{\partial \langle \rho h \rangle}{\partial t} + (\rho^l - \rho^s) h^l \frac{\partial g^s}{\partial t} + \langle \vec{v}^l \rangle \cdot \vec{\nabla} (\rho^l h^l) = \nabla \cdot (\kappa \vec{\nabla} T) \quad (5.15e)$$

$$\frac{\partial \langle \rho h \rangle}{\partial t} + \rho^l \langle \vec{v}^l \rangle \cdot \vec{\nabla} h^l = \nabla \cdot (\kappa \vec{\nabla} T) + (\rho^s - \rho^l) h^l \frac{\partial g^s}{\partial t}$$

(5.16)

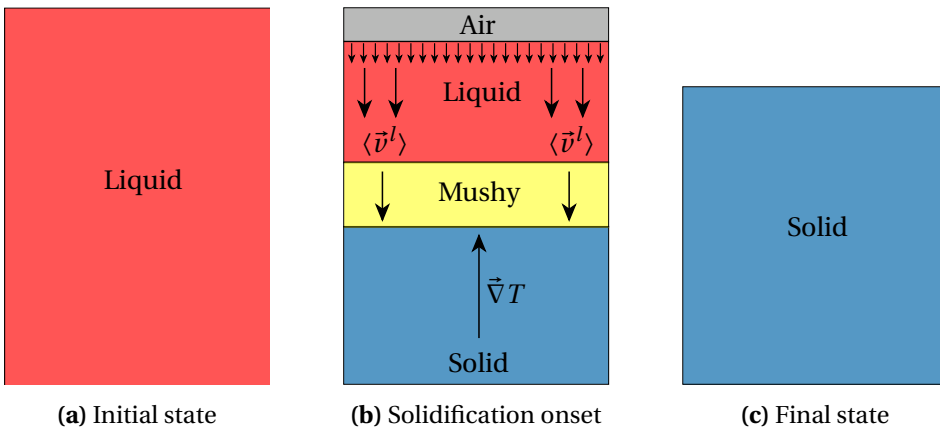


Fig. 5.2 – Effect of shrinkage flow on a solidifying ingot

Discussion

In order to keep things simple, the term "enthalpy" will refer henceforth to "volume enthalpy", otherwise, we will explicitly use the term "mass enthalpy". It is important to understand the meaning of the terms in equation (5.16). The first term in the left-hand side is the temporal change in the system's average enthalpy, i.e. a temporal change in the volume enthalpy of any of the phases in the course of solidification. The second LHS term is a dot product between the superficial liquid velocity and the the gradient of the liquid's enthalpy. Since phase densities are constant in our case, the gradient term reduces to the liquid's mass enthalpy. If we consider a representative volume element (RVE) in the liquid phase, far from the mushy zone, we can stipulate:

$$\vec{\nabla}h^l = C_p^l \vec{\nabla}T \quad (5.17)$$

assuming that the phase mass specific heat, C_p^l , is constant. Therefore, the liquid enthalpy is advected in the case where the velocity vector is not orthogonal to the temperatrate gradient. The advection reaches its maximum when the two vectors have the same direction. Consider, for instance, a filled ingot with a cooling flux applied to its bottom surface. If the density variation with temperature were to be neglected, then the sole mechanical driving force in the melt is the density jump at the solid-liquid interface ahead of the mushy zone. The temperature gradient in such a case is vertical upward, while the velocity vector is in the opposite direction. The advective term writes:

$$\rho^l \langle \vec{v}^l \rangle \cdot \vec{\nabla}h^l = -\rho^l C_p^l \|\langle \vec{v}^l \rangle\| \|\vec{\nabla}T\| \quad (5.18)$$

We see that the second RHS term in equation (5.16) acts as a heat source at the interface between the the phases, in this particular solidification scenario. Another heat power (of unit Wm^{-3}) adds to the system within the mushy, that is the second term in the right-hand side of the same equation. This term is proportional to the solidification rate. Finally, the first RHS term accounts for thermal diffusion within the phases.

It should be emphasized that the assumption of a constant specific heat in the liquid in equation (5.17) applies when no macrosegregation occurs. Nonetheless, when the latter is considered, the phases specific and latent heats become highly dependent on the local average composition. It then advisable to use the thermodynamic tabulation approach, where the enthalpies are directly tabulated as functions of temperature and composition.

5.3.4 Species Conservation

The last conservation principle is applied to the chemical species or solutes. This principle allows predicting macrosegregation when applied to a solidification system, along with the mass, momentum and energy balances. However, the conservation equation should be reformulated in the case of a melt flow driven by shrinkage.

Assumptions

- The alloy is binary, i.e., it is composed from one solute, and hence the notation of the average composition without a solute index: $\langle w \rangle$ for the mass composition and $\langle \rho w \rangle$ for the volume composition
- The solid fraction is determined assuming complete mixing in both phases, hence the lever rule is applicable. It should be mentionned that the solidification path in the current approach is tabulated using thermodynamic data at equilibrium
- The solutal diffusion coefficient D^s in the solid phase is neglected in the mass diffusive flux term. The remaining term, D^l , is a mass diffusion coefficient in the liquid phase, of unit $m^2 s^{-1}$
- Consequence of the static solid phase: $\langle \rho w \vec{v} \rangle = g^l \rho^l \langle w \rangle^l \vec{v}^l + g^s \rho^s \langle w \rangle^s \vec{v}^s = g^l \rho^l \langle w \rangle^l \vec{v}^l$

Formulation

The species conservation is pretty similar the energy conservation formulated in the previous section. For a binary alloy, we can write:

$$\frac{\partial \langle \rho w \rangle}{\partial t} + \nabla \cdot \langle \rho w \vec{v} \rangle = \nabla \cdot (\rho^l \langle D^l \rangle \vec{\nabla} \langle w \rangle^l) \quad (5.19a)$$

$$\frac{\partial \langle \rho w \rangle}{\partial t} + \nabla \cdot (g^l \rho^l \langle w \rangle^l \vec{v}^l) = \nabla \cdot (g^l \rho^l D^l \nabla \langle w \rangle^l) \quad (5.19b)$$

$$\frac{\partial \langle \rho w \rangle}{\partial t} + \rho^l \langle w \rangle^l \nabla \cdot \langle \vec{v}^l \rangle + \langle \vec{v}^l \rangle \cdot \vec{\nabla} (\rho^l \langle w \rangle^l) = \nabla \cdot (g^l \rho^l D^l \vec{\nabla} \langle w \rangle^l) \quad (5.19c)$$

$$\frac{\partial \langle \rho w \rangle}{\partial t} + \rho^l \langle w \rangle^l \frac{\rho^l - \rho^s}{\rho^l} \frac{\partial g^s}{\partial t} + \langle \vec{v}^l \rangle \cdot \vec{\nabla} (\rho^l \langle w \rangle^l) = \nabla \cdot (g^l \rho^l D^l \vec{\nabla} \langle w \rangle^l) \quad (5.19d)$$

$$\frac{\partial \langle \rho w \rangle}{\partial t} + (\rho^l - \rho^s) \langle w \rangle^l \frac{\partial g^s}{\partial t} + \langle \vec{v}^l \rangle \cdot \vec{\nabla} (\rho^l \langle w \rangle^l) = \nabla \cdot (g^l \rho^l D^l \vec{\nabla} \langle w \rangle^l) \quad (5.19e)$$

Chapter 5. Macrosegregation with solidification shrinkage

$$\frac{\partial \langle \rho w \rangle}{\partial t} + \rho^l \langle \vec{v}^l \rangle \cdot \vec{\nabla} \langle w \rangle^l = \nabla \cdot \left(\rho^l D^l \vec{\nabla} \langle w \rangle^l \right) + \left(\rho^s - \rho^l \right) \langle w \rangle^l \frac{\partial g^s}{\partial t} \quad (5.20)$$

Discussion

The species transport equation is usually derived with the volumetric average composition $\langle \rho w \rangle$, then divided by the density, which is constant if no solidification shrinkage occurs. In the case where macrosegregation is solely due to fluid flow generated by natural or forced convection, the overall volume remains constant. It is thus convenient to compute composition variations using the mass variable $\langle w \rangle$. However, in the current context, the volume is subject to changes, hence the formulation of equation (5.20) with $\langle \rho w \rangle$.

5.4 Test cases

5.4.1 Validation of LS transport

perform test case simulation of buoyancy driven air droplet in water by 2005Nagrath that I also have seen in Shyamprasad's masters report)

I read it quickly without noticing: what time step δt did they use ?

5.4.2 Shrinkage without macrosegregation

Smacs or Pseudo-Smacs test case with Level set and shrinkage

Considerations

Explain how the flow and heat transfer in the air are not important

Model equations

Give the strong form equations to be solved OR simply refer the previous section where the model was defined

Initial and boundary conditions for energy and momentum

Initially we have liquid and air at rest.

Results and discussion

Chapter 6

Macrosegregation with shrinkage and deformable solid OR Application to TEXUS

Chapter 6. Application to TEXUS

This chapter will depend on the progress in the shrinkage simulations. If everything goes with shrinkage, then maybe i can put it in Thercast and test the solid deformation also and apply to TEXUS If not then this chapter will only cover these topics:

- What are the CCEMLCC experimental facilities (ground experiments, sound rocket, ISS)
- Focus on TEXUS (setup, conditions, previous results, recent failures...)
-

Conclusion and Perspectives

Conclusions

The summary of what we did in the previous chapters

Future Work

What did we miss in our models that can be potentially important for the coming years

Appendix A

Notes

from <http://aerojet.engr.ucdavis.edu/fluenthelp/html/ug/node572.htm>

For many natural-convection flows, you can get faster convergence with the Boussinesq model than you can get by setting up the problem with fluid density as a function of temperature. This model treats density as a constant value in all solved equations, except for the buoyancy term in the momentum equation:

$$(\rho - \rho_0)g \approx -\rho_0\beta(T - T_0)g \quad (\text{A.1})$$

where ρ_0 is the (constant) density of the flow, T_0 is the operating temperature, and β is the thermal expansion coefficient. Equation 13.2-18 is obtained by using the Boussinesq approximation $\rho = \rho_0(1 - \beta\Delta T)$ to eliminate ρ from the buoyancy term. This approximation is accurate as long as changes in actual density are small; specifically, the Boussinesq approximation is valid when $\beta(T - T_0) \ll 1$.

A.1 Useful Expressions

address a problem: attend to, apply oneself to, tackle, see to, deal with, confront, come to grips with, get down to, turn one's hand to, take in hand, undertake, concentrate on, focus on, devote oneself to "the selectmen failed to address the issue of subsidies"

- the basic premise = the basic argument is that ...
- A complication inherent in this approach is that
- an important objective of the present study is to

Appendix A. Notes

Bibliography

[Auburtin et al. 2000]

Auburtin, P., T. Wang, S. L. Cockcroft, and A. Mitchell (2000). “Freckle formation and freckle criterion in superalloy castings”. *Metallurgical and Materials Transactions B*, 31 (4), pp. 801–811. URL: <http://link.springer.com/article/10.1007/s11663-000-0117-9> (cited on page 33).

[Beckermann 2002]

Beckermann, C. (2002). “Modelling of macrosegregation: applications and future needs”. *International Materials Reviews*, 47 (5), pp. 243–261. URL: <http://www.maneyonline.com/doi/abs/10.1179/095066002225006557> (cited on page 5).

[Beckermann et al. 2000]

Beckermann, C., J. P. Gu, and W. J. Boettinger (2000). “Development of a freckle predictor via rayleigh number method for single-crystal nickel-base superalloy castings”. *Metallurgical and Materials Transactions A*, 31 (10), pp. 2545–2557. URL: <http://link.springer.com/article/10.1007/s11661-000-0199-7> (cited on page 31).

[Boettinger et al. 2002]

Boettinger, W. J., J. A. Warren, C. Beckermann, and A. Karma (2002). “Phase-Field Simulation of Solidification1”. *Annual Review of Materials Research*, 32 (1), pp. 163–194. URL: <http://dx.doi.org/10.1146/annurev.matsci.32.101901.155803> (cited on page 19).

[Carozzani 2012]

Carozzani, T. (2012). “Développement d'un modèle 3D Automate Cellulaire-Éléments Finis (CAFE) parallèle pour la prédiction de structures de grains lors de la solidification d'alliages métalliques”. PhD thesis. Ecole Nationale Supérieure des Mines de Paris. URL: <http://pastel.archives-ouvertes.fr/pastel-00803282> (cited on pages 9, 26).

[Carozzani et al. 2013]

Carozzani, T. et al. (2013). “Direct Simulation of a Solidification Benchmark Experiment”. *Metallurgical and Materials Transactions A*, 44 (2), pp. 873–887. URL: <http://link.springer.com/article/10.1007/s11661-012-1465-1> (cited on pages 10, 26, 27).

[Chen et al. 1997]

Chen, S., B. Merriman, S. Osher, and P. Smereka (1997). “A Simple Level Set Method for Solving Stefan Problems”. *Journal of Computational Physics*, 135 (1), pp. 8–29. URL: <http://www.sciencedirect.com/science/article/pii/S0021999197957211> (cited on page 19).

Bibliography

[Chen 2014]

Chen, S. (2014). "Three dimensional Cellular Automaton - Finite Element (CAFE) modeling for the grain structures development in Gas Tungsten / Metal Arc Welding processes". Theses. Ecole Nationale Supérieure des Mines de Paris. URL: <https://pastel.archives-ouvertes.fr/pastel-01038028> (cited on page 20).

[Clyne et al. 1981]

Clyne, T. W. and W. Kurz (1981). "Solute redistribution during solidification with rapid solid state diffusion". *Metallurgical Transactions A*, 12 (6), pp. 965–971. URL: <http://link.springer.com/article/10.1007/BF02643477> (cited on page 15).

[Combeau et al. 1996]

Combeau, H., J.-M. Drezet, A. Mo, and M. Rappaz (1996). "Modeling of microsegregation in macrosegregation computations". *Metallurgical and Materials Transactions A*, 27 (8), pp. 2314–2327. URL: <http://link.springer.com/article/10.1007/BF02651886> (cited on page 16).

[Combeau et al. 2009]

Combeau, H., M. Založník, S. Hans, and P. E. Richy (2009). "Prediction of Macrosegregation in Steel Ingots: Influence of the Motion and the Morphology of Equiaxed Grains". *Metallurgical and Materials Transactions B*, 40 (3), pp. 289–304. URL: <http://link.springer.com/article/10.1007/s11663-008-9178-y> (cited on page 6).

[Courtois et al. 2014]

Courtois, M., M. Carin, P. L. Masson, S. Gaied, and M. Balabane (2014). "A complete model of keyhole and melt pool dynamics to analyze instabilities and collapse during laser welding". *Journal of Laser Applications*, 26 (4), p. 042001. URL: <http://scitation.aip.org/content/jia/journal/jla/26/4/10.2351/1.4886835> (cited on page 20).

[Dantzig et al. 2009]

Dantzig, J. A. and M. Rappaz (2009). *Solidification*. EPFL Press (cited on pages 2, 12, 15, 16, 25).

[Darcy 1856]

Darcy, H. (1856). *Les fontaines publiques de la ville de Dijon : exposition et application des principes à suivre et des formules à employer dans les questions de distribution d'eau*. V. Dalmont (Paris). URL: <http://gallica.bnf.fr/ark:/12148/bpt6k624312> (cited on page 13).

[Desmaison et al. 2014]

Desmaison, O., M. Bellet, and G. Guillemot (2014). "A level set approach for the simulation of the multipass hybrid laser/GMA welding process". *Computational Materials Science*, 91, pp. 240–250. URL: <http://www.sciencedirect.com/science/article/pii/S092702561400278X> (cited on page 20).

[Digonnet et al. 2007]

Digonnet, H., L. Silva, and T. Coupez (2007). "Cimlib: A Fully Parallel Application For Numerical Simulations Based On Components Assembly". *AIP Conference Proceedings*. Vol. 908. AIP Publishing, pp. 269–274. URL: <http://scitation.aip.org/content/aip/proceeding/aipcp/10.1063/1.2740823> (cited on page 10).

[DoITPoMS 2000]

DoITPoMS (2000). *Dissemination of IT for the Promotion of Materials Science*. URL: <http://www.doitpoms.ac.uk/> (cited on page 12).

[Du et al. 2001]

Du, Q., D. Li, Y. Li, R. Li, and P. Zhang (2001). "Simulating a double casting technique using level set method". *Computational Materials Science*, 22 (3–4), pp. 200–212. URL: <http://www.sciencedirect.com/science/article/pii/S0927025601001902> (cited on page 20).

[Easton et al. 2011]

Easton, M., C. Davidson, and D. StJohn (2011). "Grain Morphology of As-Cast Wrought Aluminium Alloys". *Materials Transactions*, 52 (5), pp. 842–847 (cited on page 12).

[Felicelli et al. 1991]

Felicelli, S. D., J. C. Heinrich, and D. R. Poirier (1991). "Simulation of freckles during vertical solidification of binary alloys". *Metallurgical Transactions B*, 22 (6), pp. 847–859. URL: <http://link.springer.com/article/10.1007/BF02651162> (cited on pages 6, 13).

[Flemings 1974]

Flemings, M. C. (1974). "Solidification processing". *Metallurgical Transactions*, 5 (10), pp. 2121–2134. URL: <http://link.springer.com/article/10.1007/BF02643923> (cited on page 6).

[Flemings et al. 1967]

Flemings, M. C. and G. E. Nereo (1967). "Macrosegregation: Part I". *Transactions of the Metallurgical Society of AIME*, 239, pp. 1449–1461 (cited on page 13).

[Flemings et al. 1968a]

Flemings, M. C., R. Mehrabian, and G. E. Nereo (1968a). "Macrosegregation: Part II". *Transactions of the Metallurgical Society of AIME*, 242, pp. 41–49 (cited on page 13).

[Flemings et al. 1968b]

Flemings, M. C. and G. E. Nereo (1968b). "Macrosegregation: Part III". *Transactions of the Metallurgical Society of AIME*, 242, pp. 50–55 (cited on page 13).

[Gandin 2000]

Gandin, C. A. (2000). "From constrained to unconstrained growth during directional solidification". *Acta Materialia*, 48 (10), pp. 2483–2501. URL: <http://www.sciencedirect.com/science/article/pii/S1359645400000707> (cited on page 25).

[Giamei et al. 1970]

Giamei, A. F. and B. H. Kear (1970). "On the nature of freckles in nickel base superalloys". *Metallurgical Transactions*, 1 (8), pp. 2185–2192. URL: <http://link.springer.com/article/10.1007/BF02643434> (cited on page 6).

[Gibou et al. 2003]

Gibou, F., R. Fedkiw, R. Caflisch, and S. Osher (2003). "A Level Set Approach for the Numerical Simulation of Dendritic Growth". *Journal of Scientific Computing*, 19 (1-3), pp. 183–199. URL: <http://link.springer.com/article/10.1023/A%3A1025399807998> (cited on page 19).

Bibliography

[Gouttebroze 2005]

Gouttebroze, S. (2005). "Modélisation 3d par éléments finis de la macroségrégation lors de la solidification d'alliages binaires". PhD thesis. École Nationale Supérieure des Mines de Paris. URL: <https://pastel.archives-ouvertes.fr/pastel-00001885/document> (cited on page 9).

[Hachani et al. 2012]

Hachani, L. et al. (2012). "Experimental analysis of the solidification of Sn-3 wt.%Pb alloy under natural convection". *International Journal of Heat and Mass Transfer*, 55 (7-8), pp. 1986–1996. URL: <http://www.sciencedirect.com/science/article/pii/S0017931011007009> (cited on page 27).

[Harlow et al. 1965]

Harlow, F. H. and J. E. Welch (1965). "Numerical Calculation of Time-Dependent Viscous Incompressible Flow of Fluid with Free Surface". *Physics of Fluids (1958-1988)*, 8 (12), pp. 2182–2189. URL: <http://scitation.aip.org/content/aip/journal/pof1/8/12/10.1063/1.1761178> (cited on page 19).

[Hebditch et al. 1974]

Hebditch, D. J. and J. D. Hunt (1974). "Observations of ingot macrosegregation on model systems". *Metallurgical Transactions*, 5 (7), pp. 1557–1564. URL: <http://link.springer.com/article/10.1007/BF02646326> (cited on page 27).

[Hirt 1971]

Hirt, C. W. (1971). "An arbitrary Lagrangian-Eulerian computing technique". *Proceedings of the Second International Conference on Numerical Methods in Fluid Dynamics*. Ed. by M. Holt. Lecture Notes in Physics 8. Springer Berlin Heidelberg, pp. 350–355. URL: http://link.springer.com/chapter/10.1007/3-540-05407-3_50 (cited on page 19).

[Hirt et al. 1981]

Hirt, C. W and B. D Nichols (1981). "Volume of fluid (VOF) method for the dynamics of free boundaries". *Journal of Computational Physics*, 39 (1), pp. 201–225. URL: <http://www.sciencedirect.com/science/article/pii/0021999181901455> (cited on page 19).

[Karagadde et al. 2014]

Karagadde, S., L. Yuan, N. Shevchenko, S. Eckert, and P. D. Lee (2014). "3-D microstructural model of freckle formation validated using in situ experiments". *Acta Materialia*, 79, pp. 168–180. URL: <http://www.sciencedirect.com/science/article/pii/S1359645414004984> (cited on page 33).

[Karma et al. 1996]

Karma, A. and W.-J. Rappel (1996). "Phase-field method for computationally efficient modeling of solidification with arbitrary interface kinetics". *Physical Review E*, 53 (4), R3017–R3020. URL: <http://link.aps.org/doi/10.1103/PhysRevE.53.R3017> (cited on page 19).

[Khan et al. 2014]

Khan, M. I., A. O. Mostafa, M. Aljarrah, E. Essadiqi, and M. Medraj (2014). "Influence of Cooling Rate on Microsegregation Behavior of Magnesium Alloys". *Journal of Materials*, 2014, e657647. URL: <http://www.hindawi.com/journals/jma/2014/657647/abs/> (cited on page 15).

[Kobayashi 1988]

Kobayashi, S. (1988). "Solute redistribution during solidification with diffusion in solid phase: A theoretical analysis". *Journal of Crystal Growth*, 88 (1), pp. 87–96. URL: <http://www.sciencedirect.com/science/article/pii/S0022024898900100> (cited on page 15).

[Kohler 2008]

Kohler, F. (2008). "Peritectic solidification of Cu-Sn alloys: microstructure competition at low speed". PhD thesis. EPFL (cited on page 4).

[Lesoult 2005]

Lesoult, G. (2005). "Macrosegregation in steel strands and ingots: Characterisation, formation and consequences". *Materials Science and Engineering: A, International Conference on Advances in Solidification Processes* 413–414, pp. 19–29. URL: <http://www.sciencedirect.com/science/article/pii/S0921509305010063> (cited on page 6).

[Liu 2005]

Liu, W. (2005). "Finite Element Modelling of Macrosegregation and Thermomechanical Phenomena in Solidification Processes". PhD thesis. École Nationale Supérieure des Mines de Paris. URL: <http://pastel.archives-ouvertes.fr/pastel-00001339> (cited on page 9).

[Maitre 2006]

Maitre, E. (2006). "Review of numerical methods for free interfaces". Les Houches, France. URL: <http://goo.gl/Re6f3a> (cited on page 19).

[Martorano et al. 2003]

Martorano, M. A., C. Beckermann, and C.-A. Gandin (2003). "A solutal interaction mechanism for the columnar-to-equiaxed transition in alloy solidification". *Metallurgical and Materials Transactions A*, 34 (8), pp. 1657–1674. URL: <http://link.springer.com/article/10.1007/s11661-003-0311-x> (cited on page 16).

[Mesri et al. 2009]

Mesri, Y., H. Digonnet, and T. Coupez (2009). "Advanced parallel computing in material forming with CIMLib". *European Journal of Computational Mechanics/Revue Européenne de Mécanique Numérique*, 18 (7-8), pp. 669–694. URL: <http://www.tandfonline.com/doi/abs/10.3166/ejcm.18.669-694> (cited on page 10).

[Mosbah 2008]

Mosbah, S. (2008). "Multiple scales modeling of solidification grain structures and segregation in metallic alloys". PhD thesis. École Nationale Supérieure des Mines de Paris. URL: <https://tel.archives-ouvertes.fr/tel-00349885/document> (cited on page 9).

[Ni et al. 1991]

Ni, J. and C. Beckermann (1991). "A volume-averaged two-phase model for transport phenomena during solidification". *Metallurgical Transactions B*, 22 (3), pp. 349–361. URL: <http://link.springer.com/article/10.1007/BF02651234> (cited on pages 15, 16, 22, 25).

[Osher et al. 1988]

Osher, S. and J. A. Sethian (1988). "Fronts propagating with curvature-dependent speed: Algorithms based on Hamilton-Jacobi formulations". *Journal of Computational Physics*, 79 (1),

Bibliography

pp. 12–49. URL: <http://www.sciencedirect.com/science/article/pii/0021999188900022> (cited on page 19).

[Poirier 1987]

Poirier, D. R. (1987). “Permeability for flow of interdendritic liquid in columnar-dendritic alloys”. *Metallurgical Transactions B*, 18 (1), pp. 245–255. URL: <http://link.springer.com/article/10.1007/BF02658450> (cited on page 13).

[Pollock et al. 1996]

Pollock, T. M. and W. H. Murphy (1996). “The breakdown of single-crystal solidification in high refractory nickel-base alloys”. *Metallurgical and Materials Transactions A*, 27 (4), pp. 1081–1094. URL: <http://link.springer.com/article/10.1007/BF02649777> (cited on page 33).

[Ramirez et al. 2003]

Ramirez, J. C. and C. Beckermann (2003). “Evaluation of a rayleigh-number-based freckle criterion for Pb-Sn alloys and Ni-base superalloys”. *Metallurgical and Materials Transactions A*, 34 (7), pp. 1525–1536. URL: <http://link.springer.com/article/10.1007/s11661-003-0264-0> (cited on pages 13, 33).

[Rappaz et al. 2003]

Rappaz, M., M. Bellet, and M. Deville (2003). *Numerical Modeling in Materials Science and Engineering*. Springer Series in Computational Mathematics. Springer Berlin Heidelberg (cited on pages 13, 17, 22).

[Rivaux 2011]

Rivaux, B. (2011). “Simulation 3D éléments finis des macroségrégations en peau induites par déformations thermomécaniques lors de la solidification d'alliages métalliques”. PhD thesis. École Nationale Supérieure des Mines de Paris. URL: <http://pastel.archives-ouvertes.fr/pastel-00637168> (cited on pages 9, 16, 26).

[Sarazin et al. 1992]

Sarazin, J. R. and A. Hellawell (1992). “Studies of Channel-Plume Convection during Solidification”. *Interactive Dynamics of Convection and Solidification*. Ed. by S. H. Davis, H. E. Huppert, U. Müller, and M. G. Worster. NATO ASI Series 219. Springer Netherlands, pp. 143–145. URL: http://link.springer.com/chapter/10.1007/978-94-011-2809-4_22 (cited on page 3).

[Schneider et al. 1997]

Schneider, M. C., J. P. Gu, C. Beckermann, W. J. Boettinger, and U. R. Kattner (1997). “Modeling of micro- and macrosegregation and freckle formation in single-crystal nickel-base superalloy directional solidification”. *Metallurgical and Materials Transactions A*, 28 (7), pp. 1517–1531. URL: <http://link.springer.com/article/10.1007/s11661-997-0214-3> (cited on page 3).

[Shevchenko et al. 2013]

Shevchenko, N., S. Boden, G. Gerbeth, and S. Eckert (2013). “Chimney Formation in Solidifying Ga-25wt pct In Alloys Under the Influence of Thermosolutal Melt Convection”. *Metallurgical and Materials Transactions A*, 44 (8), pp. 3797–3808. URL: <http://link.springer.com/article/10.1007/s11661-013-1711-1> (cited on pages 3, 33).

[Tan et al. 2007]

Tan, L. and N. Zabaras (2007). “A level set simulation of dendritic solidification of multi-component alloys”. *Journal of Computational Physics*, 221 (1), pp. 9–40. URL: <http://www.sciencedirect.com/science/article/pii/S0021999106002737> (cited on page 19).

[Tiller et al. 1953]

Tiller, W. A, K. A Jackson, J. W Rutter, and B Chalmers (1953). “The redistribution of solute atoms during the solidification of metals”. *Acta Metallurgica*, 1 (4), pp. 428–437. URL: <http://www.sciencedirect.com/science/article/pii/0001616053901266> (cited on page 12).

[Tourret et al. 2009]

Tourret, D. and C. A. Gandin (2009). “A generalized segregation model for concurrent dendritic, peritectic and eutectic solidification”. *Acta Materialia*, 57 (7), pp. 2066–2079. URL: <http://www.sciencedirect.com/science/article/pii/S1359645409000184> (cited on page 16).

[Wang et al. 1993]

Wang, C. Y. and C. Beckermann (1993). “A multiphase solute diffusion model for dendritic alloy solidification”. *Metallurgical Transactions A*, 24 (12), pp. 2787–2802. URL: <http://link.springer.com/article/10.1007/BF02659502> (cited on page 16).

[Xu et al. 1991]

Xu, D. and Q. Li (1991). “Gravity- and Solidification-Shrinkage-Induced Liquid Flow in a Horizontally Solidified Alloy Ingot”. *Numerical Heat Transfer, Part A: Applications*, 20 (2), pp. 203–221. URL: <http://dx.doi.org/10.1080/10407789108944817> (cited on page 13).

[Yuan et al. 2012]

Yuan, L. and P. D. Lee (2012). “A new mechanism for freckle initiation based on microstructural level simulation”. *Acta Materialia*, 60 (12), pp. 4917–4926. URL: <http://www.sciencedirect.com/science/article/pii/S1359645412003205> (cited on page 33).